A MULTISCALE MODEL FOR THE OXIDE ION CONDUCTING AND PROTON CONDUCTING SOLID OXIDE CELLS

BY

LINJIAN MA

THESIS

Submitted in partial fulfillment of the requirements
for the degree of Master of Science in Mechanical Engineering
with a concentration in Computational Science and Engineering
in the Graduate College of the
University of Illinois at Urbana-Champaign, 2018

Urbana, Illinois

Adviser:

Professor Narayana R. Aluru

ABSTRACT

Solid oxide cells (SOCs) are high-efficiency energy conversion devices under high temperature. However, the key reaction mechanisms governing the overall performance of SOCs are not well understood. Here, we develop a multiscale model combining density functional theory calculations, transition state theory and continuum modeling to elucidate the essential reaction steps and predict the performance of the device. Density functional theory calculations are used to obtain the free energy barriers for different reaction steps, transition state theory is used to predict the reaction rate constants for each step based on the free energy barriers, and the continuum theory utilizes the reaction rate constants to obtain the voltage loss-current density relations. We apply the methodology to both the oxide ion-conducting SOCs as well as the proton-conducting SOCs. The proposed multiscale model yields quantitative agreement with the voltage loss-current density data from experiments. The results indicate that as to the oxygen electrode reactions in the Lanthanum Strontium Cobalt Ferrite ($La_{1-x}Sr_xCo_{1-y}Fe_yO_{3-\delta}$ or LSCF) based oxide ion-conducting SOCs, the reaction step involving the splitting of the surface oxygen molecules into oxide ions under SOFC mode and the combination of surface oxide ions into oxygen molecules under SOEC mode is the rate limiting reaction step, and the diffusion of oxide ions in bulk LSCF is the rate limiting diffusion step. As to the Pt/Y-doped $BaZrO_3$/Ag based proton-conducting SOFC, the cathode reactions are rate-limiting steps.

Key Words: multiscale modeling, continuum modeling, transition state theory, density functional theory, solid oxide cells

To my parents, for their love and encouragement.
To my friends, for their help and support.

ACKNOWLEDGMENTS

I deeply thank Professor Narayana R. Aluru for his guidance over the last two years. This work was done under his supervision. During the time when I was struggled with the problems, his comments and suggestions could always give me inspirations to find the answers. His deep understanding of the physical meaning of the concepts and problems stimulated me a lot.

I thank my group members Yuhang Jing and Tao Sun, who gave me important suggestions about quantum calculations.

Last but most importantly, I am deeply grateful to my parents who have raised me and always been supportive. They always encourage and trust me whatever situation or difficulty I encounter. It would not have been possible for me to come to this stage of my life without their unchanging love and unlimited support.

TABLE OF CONTENTS

LIST OF TABLES

LIST OF FIGURES

LIST OF ABBREVIATIONS

SOCs	Solid Oxide Cells
SOFC	Solid Oxide Fuel Cell
SOEC	Solid Oxide Electrolysis Cell
MIEC	Mixed Ionic-Electronic Conductors
LSCF	Lanthanum Strontium Cobalt Ferrite
GDC	Gadolinium doped Ceria
BZY	Yttrium doped Barium Zirconate
DFT	Density Functional Theory
TST	Transition State Theory
TPB	Triple Phase Boundary

LIST OF SYMBOLS

k	Reaction rate constant
D	Diffusivity
C	Concentration of different species
G	Gibbs free energy
F	Helmholtz free energy
P	Pressure of gas
V	Volume of the gas
Z	Partition function
v	Vibrational frequency
E_0	Electronic internal energy under 0K
S	Entropy
r	Reaction rates for different reaction steps
φ	Electric potential
σ	Electronic conductivity
I	Current density
η	Overpotential
k_B	Boltzmann constant
T	Temperature
h	Planck's constant
λ	Jump length of a diffusion step

z	Number of first neighbors in the diffusion step, which is 2 in 1D diffusion, 4 on a square lattice, and 6 on a hexagonal lattice
ϕ	Porosity
τ	Tortuosity
F_a	Faraday's constant
χ	The electrostatic potential difference at the LSCF/gas interface
S_e	Sensitivity of current density
P_a	Parameters in sensitivity analysis
a	The parameter representing the free energy deviation from the ideal structure
d	Vertical distance between the uppermost oxygen and the surface layer
ϵ	Permittivity of the material
e	Charge of an electron
I_m	Moment of Inertia
α	Charge transfer coefficient
$\Delta G_{f,vac}$	Vacancy formation free energy
V_O	The oxygen vacancy in bulk LSCF
A	Material's surface area

CHAPTER 1

INTRODUCTION

1.1 Background

Hydrogen is a clean and sustainable fuel compared with fossil fuels such as coal and petroleum, since it does not produce harmful gases and could be produced through water electrolysis[3]. Developing environmentally friendly and highly efficient processes to utilize as well as to generate hydrogen is of great interest. Solid oxide cells (SOCs) are high-efficiency energy conversion devices for generation of electricity or production of hydrogen under high temperature[4]. They can work under fuel cell mode (SOFC) to transform hydrogen and oxygen into water steam and produce electricity[5, 6, 7], as well as function under electrolysis cell mode (SOEC) to consume electricity and produce hydrogen from water[3, 8, 9]. SOCs have attracted wide attention due to their high performance.

Typical SOCs have three components, one dense electrolyte and two porous electrodes. Stable oxide ion conductors, such as Yttria-Stabilized Zirconia (YSZ) and Strontium, Magnesium doped Lanthanum Gallate (LSGM), are normally used as electrolytes[7, 9, 10, 11]. Transition metals, such as Pt and Ni, are widely used as the hydrogen electrodes. Mixed Ionic-Electronic Conductors (MIEC) such as $La_{1-x}Sr_xCo_{1-y}Fe_yO_{3-\delta}$ (LSCF)[7, 12] are typically used as the oxygen electrodes. Since YSZ is an oxide ion-conducting material, this kind of SOCs is called oxide ion-conducting SOCs. Typically, the oxygen electrode polarization resistance in oxide ion-conducting SOCs is high and is a primary impediment for high cell efficiency[7, 13, 14]. Understanding the reaction mechanisms and rate-limiting steps in the oxygen electrode is essential for improving the efficiency.

Compared to oxide ion-conducting SOCs, proton-conducting SOCs offer many advantages in several perspectives. First, proton conductors have

higher ionic conductivity compared with that of oxide ion conductors in the intermediate temperature range, resulting in high cell efficiency[15, 16]. Second, many proton-conducting materials show better chemical compatibility with Ni, which is a commonly used hydrogen electrode for SOFCs[17]. Therefore, it is essential to understand the working mechanisms in proton-conducting SOCs and design efficient proton-conducting devices.

1.2 Motivation for Modeling of Oxide Ion-Conduction SOCs

As stated above, understanding the reaction mechanisms and rate-limiting steps in the oxygen electrode is essential for improving the efficiency. The reaction equation for the oxygen electrode under SOFC mode is

$$0.5O_2 + 2e^- \rightarrow O^{2-}$$

And the reaction equation under SOEC mode is

$$O^{2-} \rightarrow 0.5O_2 + 2e^-$$

The large polarization resistance in the oxygen electrode is due to the slow reaction rates of these two reactions. To lower the resistance, MIECs are used as oxygen electrodes, since oxygen release or incorporation can be extended to the entire electrode surface rather than only near the Triple Phase Boundary (TPB). LSCF, a typical MIEC material, is a p-type semiconductor with electronic and ionic conductivity[1]. It is widely-used as an oxygen electrode because of its high stability, good catalytic ability for oxygen reactions and low oxide ion conducting resistance[18, 19, 20]. Understanding the LSCF based oxygen electrode reaction mechanisms is essential for designing efficient and effective SOCs.

To investigate the reaction mechanisms in LSCF based electrode, both computational and experimental studies have been conducted. Current density-overpotential curves and overall reaction rates can be obtained through experiments, but it is difficult to obtain detailed insights into chemical reactions

via experiments, thereby limiting the approaches one could pursue to improve the efficiency of the whole cell[21, 22, 23]. First principle calculations, including density functional theory (DFT) and ab initio molecular dynamics (AIMD), can provide detailed insights into the chemical reactions occuring in the electrode[20, 24, 25, 26, 27, 28, 29]. However, the high computational cost restricts the system to fewer than 200 atoms, which is inadequate to describe the physics of the entire cell. Furthermore, much work has been done on understanding the importance of each reaction step using continuum modeling[1, 30, 31]. For example, Adler, Lane and Steele developed a continuum model to explain the oxygen reduction pathways in MIEC[30]. Fleig developed a charge transfer model for the MIEC surface[32]. Yurkiv et al. developed a model whose impedance spectrum results were consistent with experiments[31]. While these results helped explain the reaction mechanisms in LSCF, the fitted values for important physical parameters, such as reaction rate constants and diffusivities, used in the continuum models lower their reliability. Therefore, it is essential to build a more reliable model incorporating realistic models for various physical parameters.

1.3 Motivation for Modeling of Proton-Conduction SOCs

The anode reaction equation for the proton-conducting SOFCs is

$$\mathrm{H_2} \longrightarrow 2\mathrm{H^+} + 2\mathrm{e^-}$$

And the cathode reaction equation is

$$0.5\mathrm{O_2} + 2\mathrm{H^+} + 2\mathrm{e^-} \longrightarrow \mathrm{H_2O}$$

Metals, such as Ni, Pt and Ag, are commonly used as electrodes, and proton-conducting materials, such as Y-doped $BaZrO_3$ and Y-doped $SrZrO_3$, are commonly used as electrolytes. Many chemical reactions happen on the surface of electrodes, at the TPB, and in the bulk electrolyte. Understand-

ing proton-conducting SOFC reaction mechanisms is essential for designing efficient and effective cells.

To investigate the reaction mechanisms in the proton-conducting SOFC, both computational and experimental studies have been conducted. Current density-voltage loss curves and overall reaction rates can be obtained through experiments, but it is difficult to obtain detailed insights into chemical reactions via experiments, thereby limiting the approaches one could pursue to improve the efficiency of the whole cell[2]. First principle calculations as well as atomic scale calculations, including density functional theory (DFT) and reactive force field molecular dynamics (ReaxFF), can provide detailed insights into the chemical reactions occurring in the electrode[33, 34, 35, 36]. However, the high computational cost restricts the simulation length scale and is inadequate to describe the physics of the entire cell. Furthermore, some work has been done on understanding the importance of each reaction step using continuum simulations[9]. However, the fitted values for important physical parameters lower their reliability. Therefore, it is essential to build a more reliable model incorporating realistic models for various physical parameters.

1.4 Thesis Overview

In this work, we develop a multiscale approach combining DFT-based quantum scale simulations, transition state theory (TST) and continuum scale simulations to elucidate the essential reaction steps and predict the performance of the SOCs. First, DFT-based calculations are performed to calculate the energy barriers for each reaction step and the vibrational frequencies of atoms, to obtain the free energy landscape of the entire reaction processes. These results are used in the TST to obtain the reaction rate constants and diffusivities. These results are subsequently used in the continuum theory to calculate the current density–voltage loss curves which are compared with the experimental data. We apply the methodology to both the oxygen electrode in the oxide ion-conducting SOCs as well as the proton-conducting SOFCs.

Chapter 2 introduces the overall multiscale simulation details. First, simulation setups of DFT-based calculations are presented. Second, details of TST and the methods for free energy calculations are presented. Third, the

governing transport equation for continuum modeling is presented.

Chapter 3 introduces the details for modeling of the oxygen electrode in the oxide ion-conducting SOCs. First, the model structure and the overall reaction steps are presented. Second, Simulation details, including simulation structures in DFT+U calculations and detailed equations in continuum modeling are presented. Third, the simulation results for DFT+U calculations as well as continuum modeling are presented.

Chapter 4 introduces the details for modeling of proton-conducting SOFCs. First, the model structure and the overall reaction steps are presented. Second, Simulation details, including simulation structures in DFT calculations and detailed equations in continuum modeling are presented. Third, the simulation results for DFT calculations as well as continuum modeling are presented.

Chapter 5 summarizes the major accomplishments of the thesis.

CHAPTER 2

MULTISCALE FRAMEWORK

The overall multiscale framework is presented in Figure 2.1 and is discussed in more detail in the following sections.

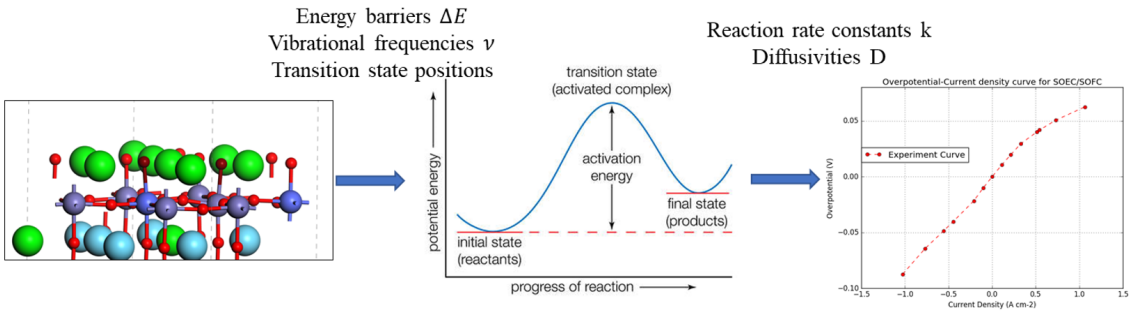

Figure 2.1: Schematic representation of the multiscale framework. The left picture is one structure in DFT-based calculations. The middle picture shows the energy diagram used in the TST. The right picture is the current density–overpotential curve.

2.1 Density Functional Theory Calculations

We used Vienna Ab initio simulation package (VASP)[37, 38, 39], version 5.3.5 to perform all spin-polarized DFT+U calculations with periodic boundary conditions[40, 41, 42]. Generalized gradient approximation (GGA) exchange-correlation functional of Perdew-Burke-Ernzerhof (PBE)[43] was used, and the conjugate-gradient method was utilized to optimize the ionic positions until the Hellmann-Feynman forces on each ion were less than 0.04 eV/Å. The energy convergence criterion was 10^{-5} eV. The plane wave basis set cutoff energy was set to be 500 eV. The projector augmented wave (PAW) method was used to calculate the interactions between valance electrons and nuclei plus core electrons[44, 45].

The rotationally invariant formulation was used for the U terms to describe the electron-electron interactions in the 3d orbitals of Fe, Co atoms and 4f orbitals of Ce, Gd atoms[41]. In this formulation, only the differences (U_{eff}) between the Coulomb (U) and exchange (J) values were the inputs of the calculations. The U_{eff} values for Fe, Co were chosen to be 4.0 eV[46, 47, 48], and for Ce, Gd were chosen to be 5.0 eV[49], which were recommended in the literature. The migration energy barriers and the transition state (TS) positions were calculated using the climbing image nudged elastic band method (CI-NEB)[50]. Bader charge analysis was performed to calculate the atomic charges[51]. We used a $4 \times 4 \times 4$ Monkhorst-Pack[52] k-point mesh for bulk systems, and used a $4 \times 4 \times 1$ Monkhorst-Pack k-point mesh for surface and interface systems.

2.2 Transition State Theory

Accurate parameters for reaction rate constants and diffusivities are needed to perform continuum calculations. Some of them can be obtained from existing literature, for example, diffusivities of O_2 in gas phase and O^{2-} in bulk LSCF[1, 53, 54], while other parameters need to be calculated using transition state theory. The equations relating reaction rate constants, diffusivities and free energy barriers are given by:

$$\begin{aligned} k &= \frac{k_B T}{h} \exp(-\frac{\Delta G(T,C)}{k_B T}) \\ D &= \frac{\lambda^2}{z} \frac{k_B T}{h} \exp(-\frac{\Delta G(T,C)}{k_B T}) \end{aligned} \tag{2.1}$$

where k denotes the reaction rate constant, D denotes the diffusivity, k_B denotes the Boltzmann constant, T denotes the temperature, C denotes the concentration of different species, h denotes the Planck's constant, and G denotes the Gibbs free energy.

The free energy barriers are a function of temperature and concentration of ions. Assuming the influences of temperature and concentration on barriers are independent of each other, we have

$$\Delta G(T,C) = \Delta G(T) + \Delta G(C) \tag{2.2}$$

The expressions for $\Delta G(C)$ will be discussed in Section 3.3.2, Influence of Concentration Variation on Free Energy Barriers. In other situations, this term has minor effect on the overall reaction rates/diffusivities and is neglected.

For the molecules in gas phase (O_2, H_2 and H_2O molecules), the temperature-dependent Gibbs free energy is expressed as

$$\begin{aligned} G_i(T) &= F_i^{0K} + F_i^{translation} + F_i^{rotation} + F_i^{vibration} + (PV)_i \\ &= -k_B T \ln Z_i^{0K} - k_B T \ln Z_i^{tr} - k_B T \ln Z_i^{rot} - k_B T \ln Z_i^{vib} + (PV)_i \end{aligned} \tag{2.3}$$

$$\begin{aligned} Z_i^{0K} &= 3\exp(-\frac{E_{0,i}}{k_B T}) \\ Z_i^{tr} &= (\frac{2\pi m k_B T}{h^2})^{\frac{3}{2}} V \\ Z_i^{rot} &= (\frac{8\pi^2 I_m k_B T}{2h^2}) \\ Z_i^{vib} &= (\frac{\exp(-\frac{h\nu_i}{2k_B T})}{1-\frac{h\nu_i}{k_B T}}) \end{aligned} \tag{2.4}$$

where F denotes the Helmholtz free energy, P denotes the pressure, V denotes the volume, Z denotes the partition function. Derivations of these equations are from reference [55].

For the adsorbed molecules (adsorbed O_2, H_2 and H_2O on material surfaces), the Gibbs free energy can be expressed as

$$\begin{aligned} G_{i_{ads}}(T) =& F_{i_{ads}} + (PV)_i \\ F_{i_{ads}} =& E_{0,i_{ads}} + \frac{7}{2}k_B T - T S_{i_{ads}} \end{aligned} \tag{2.5}$$

For the adsorbed gas, the following approximations are used to obtain the entropy term $S_{O_{2,ads}}$[56, 57]:

$$\begin{aligned} S_{i_{ads}} &\approx 0.7 S_i - 3.3 k_B \\ S_i &= \frac{1}{T}(E_{0,i} + \frac{7}{2}k_B T - F_i) \end{aligned} \tag{2.6}$$

For the ions (O^{2-}, H^+,OH^- and so on), the Gibbs free energy can be expressed as

$$
\begin{aligned}
G_i(T) \approx F_i = & F_i^{0K} + F_i^{vibration} \\
F_i^{0K} = & E_{0,i} \\
F_i^{vibration} = & 0.5 \sum_{m=1}^{3N} h\nu_m + k_B T \sum_{m=1}^{3N} \ln(1 - \exp(-\frac{h\nu_m}{k_B T}))
\end{aligned}
\tag{2.7}
$$

The terms $E_{0,i}$ are the internal energies of each species at 0K. These terms are calculated using DFT-based calculations. The vibrational frequencies are calculated using the finite displacement method. All atoms in reaction or diffusion process and their nearest neighbor atoms were included in the calculations, as they are directly involved in the reaction mechanism[58]. The vibrational frequencies at a constant volume were obtained within the harmonic approximation using finite ionic displacements $\pm 0.015 \mathring{A}$.

2.3 Continuum Modeling

In continuum scale, the current density output is coming from the transport of ions. Here we use the continuum scale transport equations to describe this phenomenon:

$$
\frac{d}{dz}[-\frac{\phi}{\tau} D_i (\frac{d}{dz} C_i - \frac{F_a C_i}{RT} \frac{d}{dz} \varphi)] = 2 r_i \tag{2.8}
$$

where i denotes different species, C denotes the concentration of different species, r denotes the reaction rates, φ denotes the electric potential, D denotes the diffusivity, ϕ denotes the porosity, τ denotes the tortuosity, F_a denotes the Faraday's constant, T denotes the temperature, and R denotes the ideal gas constant. The expressions for electric field, $-\frac{d}{dz}\varphi$, reaction rates r and boundary conditions will be presented in later chapters.

CHAPTER 3

MODELING OF OXIDE ION-CONDUCTING SOLID OXIDE CELLS

In this chapter, we develop a multiscale approach combining DFT-based quantum scale simulations, transition state theory and continuum scale simulations to determine the key reaction/diffusion steps in the LSCF-based electrode. Our results are consistent with the experimental data. We also investigate the sensitivity of the current density-overpotential curve to reaction rate and diffusion parameters and determine the key reaction/diffusion steps.

3.1 Model Structure and Reaction Steps

The overall structure modeled in the chapter is the same as that in reference[1] and shown in Figure 3.1. The $23\mu m$ electrode is the porous LSCF structure ($La_{0.6}Sr_{0.4}Co_{0.2}Fe_{0.8}O_{3-\delta}$), and the electrolyte is the dense Gadolinium doped Ceria (GDC). The upper boundary of the electrode is exposed to the pure oxygen gas under 1 atm pressure, and the lower boundary interface with the electrolyte. All the reactions are at 1073K, which is the same temperature as in experiments. The entire oxygen reduction reactions for LSCF-based SOFC are shown in Figure 3.1. The SOEC mode reactions are the reverse process of those shown for the SOFC mode. The entire oxygen reduction process can be separated into 5 transport steps (T1 to T5) and 6 reaction steps (R1 to R6) and are presented below:

The 5 transport steps:

1. Transport of O_2 in gas phase (T1).
2. Transport of $O_{2,ads}$ on LSCF surface (T2).
3. Transport of $O^{2-}_{2,suf}$ on LSCF surface (T3).

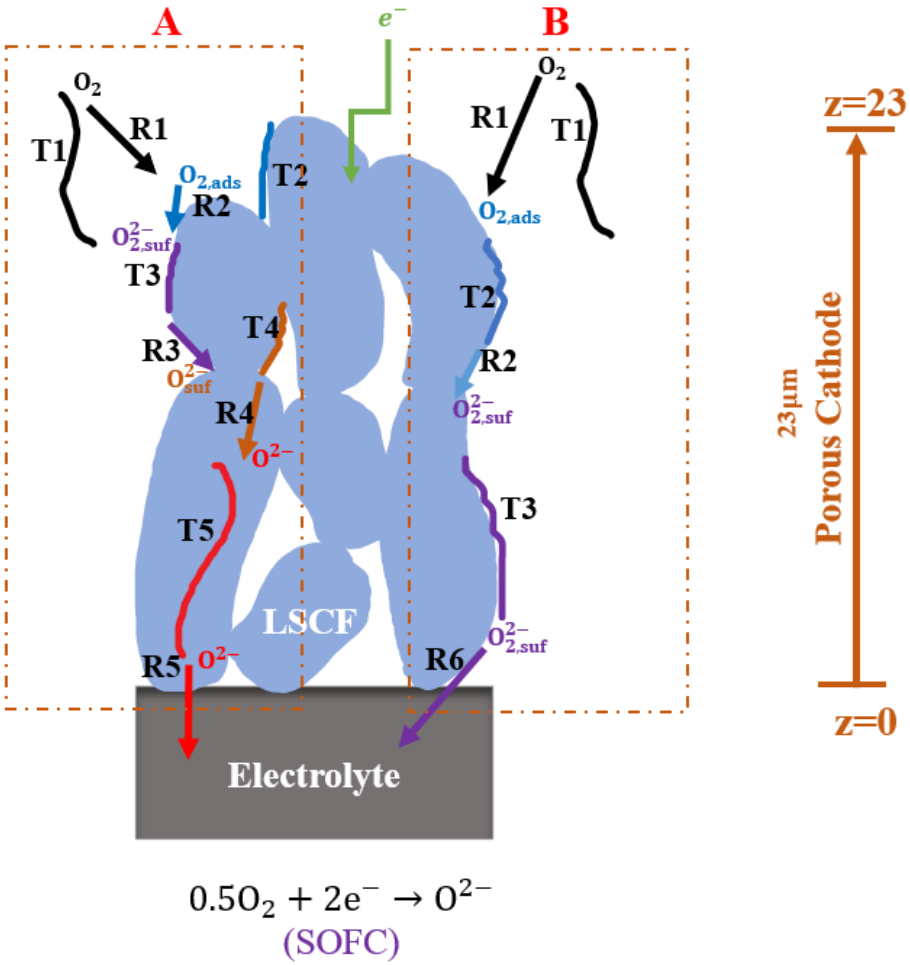

Figure 3.1: Schematic representation of the reactive pathways in the model (presented in SOFC mode). The blue grains are the LSCF phase, the white spaces between them are the gas phase, and the gray rectangle is the GDC phase. Oxygen can transport into the electrolyte through the bulk LSCF phase, which is shown in the left part of the figure and denotes path A, or transport into the electrolyte through the TPB, which is shown in the right part of the figure and denotes path B. The reactive pathways under SOEC mode are the reverse process of that for SOFC.

4. Transport of O^-_{suf} on LSCF surface (T4).

5. Transport of O^{2-} in bulk LSCF (T5).

where $O_{2,ads}$ denotes the adsorbed O_2 molecule on the LSCF surface, $O^{2-}_{2,suf}$ denotes the oxygen molecule on the LSCF surface with 2 extra electrons, O^-_{suf} denotes the oxide ion on the LSCF surface, O^{2-} denotes the oxide ion in bulk LSCF.

The 6 reaction steps:

1. Adsorption of O_2 on LSCF surface (R1):

$$\mathrm{O_2 \longrightarrow O_{2,ads}}$$

2. $O_{2,ads}$ fills vacancies on LSCF surface (R2):

$$\mathrm{O_{2,ads} + V_O^{suf} + 2e^- \longrightarrow O_{2,suf}^{2-}}$$

3. Splitting of $O^{2-}_{2,suf}$ into two O^-_{suf} on LSCF surface (R3):

$$\mathrm{O_{2,suf}^{2-} + V_O^{suf,n} \longrightarrow 2O_{suf}^-}$$

4. O^-_{suf} transports to the bulk LSCF (R4):

$$\mathrm{O_{suf}^- + V_O + e^- \longrightarrow V_O^{suf} + O^{2-}}$$

5. O^{2-} transports across the interface between LSCF and electrolyte (R5):

$$\mathrm{O^{2-} + V_O^{ele} \longrightarrow O_{ele}^{2-} + V_O}$$

6. $O^{2-}_{2,suf}$ transports across the TPB (R6):

$$\mathrm{O_{2,suf}^{2-} + V_O^{ele} + e^- \longrightarrow O_{ele}^{2-} + O_{suf}^-}$$

where V_O^{suf} denotes the oxygen vacancy on the LSCF surface, $V_O^{suf,n}$ denotes the V_O^{suf} that is neighboring to $O_{2,suf}^{2-}$, V_O^{ele} denotes the oxygen vacancy in bulk electrolyte, O_{ele}^{2-} denotes the oxide ion in bulk electrolyte (GDC). It should be noted that oxygen can transport into the electrolyte through both LSCF/GDC interface or the three-phase boundary as shown in Figure 3.1.

3.2 Simulation Details

3.2.1 DFT+U Calculations

$La_{0.6}Sr_{0.4}Co_{0.2}Fe_{0.8}O_{3-\delta}$ is the material used in the experiments. To minimize the structure difference between the simulation and experiment, we focused on the structure $La_{0.625}Sr_{0.375}Co_{0.25}Fe_{0.75}O_{3-\delta}$, which has already been discussed in previous work[20, 48]. The relaxed LSCF bulk structure used in the calculations is the supercell with $2\sqrt{2} \times 2\sqrt{2} \times 2$ unit cells, and is shown in Figure 3.2(a-b). The lattice parameters are a=b=c=3.843 Å, and $\alpha = \beta = \gamma = 90°$, same as those in reference [20]. The overall bulk LSCF structure is consistent with the normal ABO_3 structure for perovskites (A=La, Sr, B=Co, Fe). To confirm that the structure is suitable for subsequent calculations, we calculated the vacancy formation energy in the structure:

$$\Delta E_{f,vac} = E_{defective} + 0.5E_{O_2} - E_{host} \tag{3.1}$$

where $\Delta E_{f,vac}$ is the vacancy formation energy, $E_{defective}$ is the total energy of the bulk LSCF with one oxygen vacancy, E_{host} is the total energy of the perfect bulk LSCF, and E_{O_2} is the energy of an oxygen molecule[48]. The oxygen vacancies were located at different positions in bulk LSCF, and the calculated vacancy formation energies are within the range of [0.95,1.44] eV, consistent with the previous experimental results[59, 60, 61, 62, 63].

The LSCF surface structure used in the calculations is shown in Figure 3.2(c-d). Here we used a (100) oriented 6-layer slab, as this surface is the most stable one[20]. A vacuum slab larger than $15\mathring{A}$ was used above the surface to minimize the interactions between the surface structure and its periodic images. The bottom layer atoms were fixed at the bulk position,

while the rest of the atoms were fully relaxed. The first, third and fifth layers are the AO layers, and the second, fourth and sixth layers are the BO_2 layers. For the cases considered, the surface layer has the SrO-terminated structure, since Sr termination on annealed LSCF surface is an important observation in experiments[64].

The LSCF/GDC interface structure used in the calculations is shown in Figure 3.2(e-f). Here we used a (100) oriented 5-layer slab for LSCF phase, and a (100) oriented 3-layer slab for GDC phase. As LSCF and GDC have similar lattice parameters, the GDC structure is also chosen to be (100) oriented, and that orientation can form a stable interface with (100) oriented LSCF. The lattice parameters are a=b=c=3.834Å, which are the average lattice length for LSCF and GDC, and $\alpha = \beta = \gamma = 90°$. A vacuum slab larger than $15\mathring{A}$ was used to minimize the interactions between the interface structure and its images. The bottom layer atoms were fixed at the bulk position, the upper layer atoms were fixed at the bulk position along directions perpendicular to the slab, while the rest of the atoms were fully relaxed. Due to the Sr segregation phenomenon at interface shown in the experiments[65, 66, 67], the fifth atom layer, which is the interfacial layer between the two materials (shown in Figure 3.2(e)), is chosen to be SrO layer.

3.2.2 Continuum Modeling

The entire oxygen reduction process is separated into 5 transport steps and 6 reaction steps, as stated above. Here a 1-D continuum model is used to describe them. The 5 transport equations are as follows:

Transport of O_2 in gas phase (T1):

$$\frac{d}{dz}(-\frac{\phi_{gas}}{\tau_{gas}}D_{O_2}\frac{d}{dz}C_{O_2}) = -r_{R1}^{suf} \tag{3.2}$$

Transport of $O_{2,ads}$ on LSCF surface (T2):

$$\frac{d}{dz}(-\frac{\phi_{gas}}{\tau_{gas}}D_{O_{2,ads}}\frac{d}{dz}C_{O_{2,ads}}) = r_{R1}^{suf} - r_{R2}^{suf} \tag{3.3}$$

Transport of $O_{2,suf}^{2-}$ ion on LSCF surface (T3):

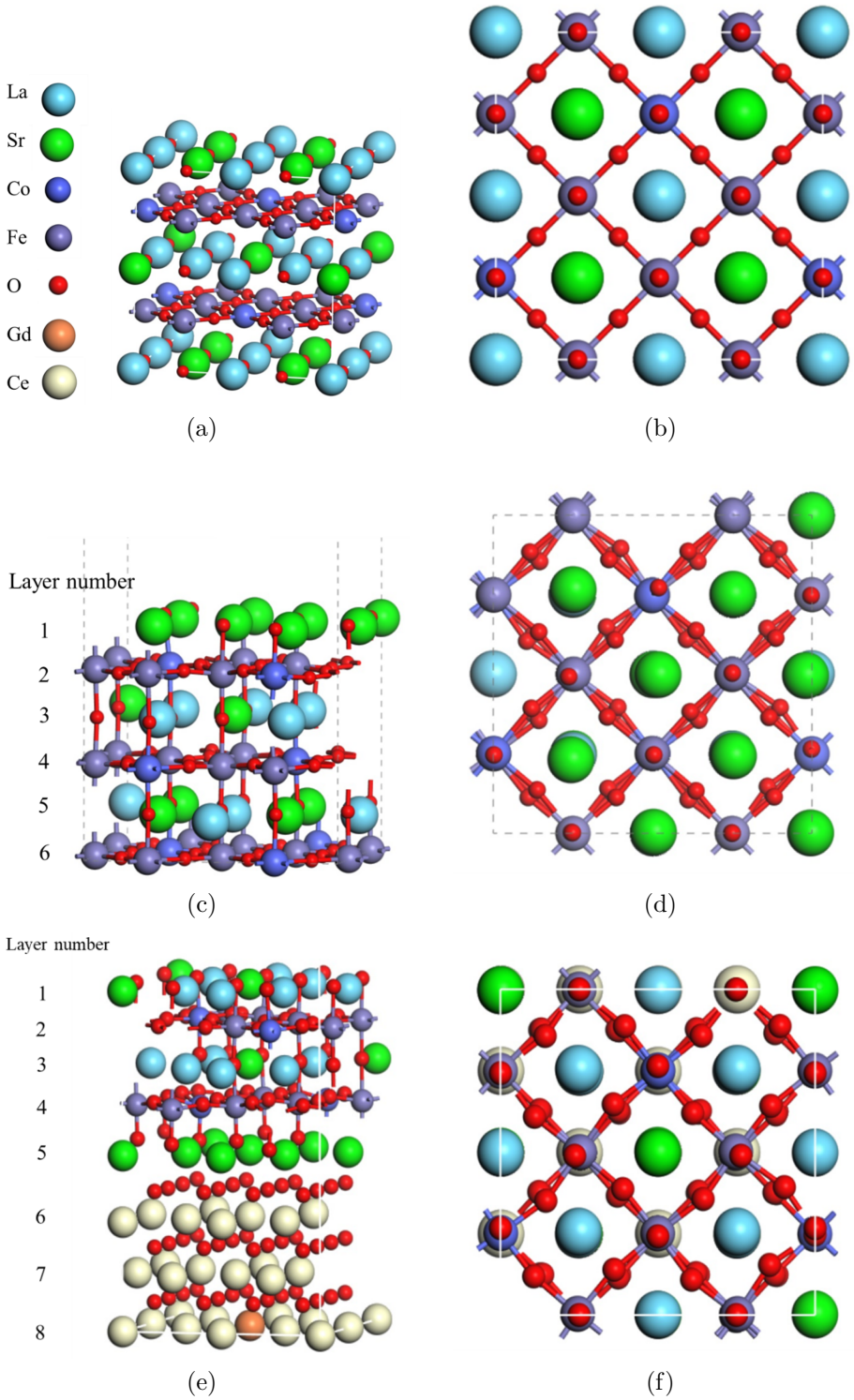

Figure 3.2: The structures used in the DFT+U calculations. The structures shown in the figures are all after structural relaxation. (a-b) Side and top view of the LSCF bulk structure. (c-d) Side and top view of the LSCF surface structure. (c-d) Side and top view of the LSCF/GDC interface structure.

$$\frac{d}{dz}[-\frac{\phi_{LSCF}}{\tau_{LSCF}}D_{O^{2-}_{2,suf}}(\frac{d}{dz}C_{O^{2-}_{2,suf}}-\frac{2F_aC_{O^{2-}_{2,suf}}}{RT}\frac{d}{dz}\varphi)]=r^{suf}_{R2}-r^{suf}_{R3} \tag{3.4}$$

Transport of O^{-}_{suf} ion on LSCF surface (T4):

$$\frac{d}{dz}[-\frac{\phi_{LSCF}}{\tau_{LSCF}}D_{O^{-}_{suf}}(\frac{d}{dz}C_{O^{-}_{suf}}-\frac{F_aC_{O^{-}_{suf}}}{RT}\frac{d}{dz}\varphi)]=2r^{suf}_{R3}-r^{suf}_{R4} \tag{3.5}$$

Transport of O^{2-} ion in bulk LSCF (T5):

$$\frac{d}{dz}[-\frac{\phi_{LSCF}}{\tau_{LSCF}}D_{O^{2-}}(\frac{d}{dz}C_{O^{2-}}-\frac{2F_aC_{O^{2-}}}{RT}\frac{d}{dz}\varphi)]=r^{suf}_{R4} \tag{3.6}$$

Experimental values for ϕ_{gas},τ_{gas},ϕ_{LSCF},τ_{LSCF} are in Table 3.1. As is shown in Figure 3.1, the boundary conditions at the top and the bottom of the electrode are as follows:

Top boundary (z=23 μm):

$$\begin{aligned} C_{O_2}&=\frac{p}{RT}\\ \frac{d}{dz}C_{O_{2,ads}}&=0\\ \frac{d}{dz}C_{O^{2-}_{2,suf}}&=0\\ \frac{d}{dz}C_{O^{-}_{suf}}&=0\\ \frac{d}{dz}C_{O^{2-}}&=0 \end{aligned} \tag{3.7}$$

Bottom boundary (z=0 μm):

$$\begin{aligned} \frac{d}{dz}C_{O_2}&=0\\ \frac{d}{dz}C_{O_{2,ads}}&=0\\ -D_{O^{2-}_{2,suf}}\frac{d}{dz}C_{O^{2-}_{2,suf}}&=-r^{TPB}_{R6}\\ -D_{O^{-}_{suf}}\frac{d}{dz}C_{O^{-}_{suf}}&=r^{TPB}_{R6}\\ -D_{O^{2-}}\frac{d}{dz}C_{O^{2-}}&=-r^{int}_{R5} \end{aligned} \tag{3.8}$$

The expression for the electric potential gradient is as follows:

$$\frac{d}{dz}\varphi = \frac{2F_a D_{O^{2-}}(\frac{d}{dz}C_{O^{2-}} - \frac{d}{dz}C_{O^{2-}}(bottom))}{\sigma + \frac{4{F_a}^2 C_{O^{2-}} D_{O^{2-}}}{RT}} \tag{3.9}$$

The derivation of equation (3.9) is presented in Appendix A.

The reaction rate expressions for R1-R6 are as follows:

For reaction R1:

$$r_{R1}^{suf} = A_{suf}[k_{1,suf}^{+} C_{O_2} - k_{1,suf}^{-} C_{O_{2,ads}}] \tag{3.10}$$

For reaction R2:

$$\begin{aligned} r_{R2}^{suf} &= A_{suf}[k_{2,suf}^{+} C_{O_{2,ads}} \frac{C_{V_O^{suf}}}{C_{O_{suf}^{2-}}^{max}} - k_{2,suf}^{-} C_{O_{2,suf}^{2-}}] \\ C_{V_O^{suf}} &= C_{O_{suf}^{2-}}^{max} - C_{O_{2,suf}^{2-}} - C_{O_{suf}^{-}} \end{aligned} \tag{3.11}$$

For reaction R3:

$$\begin{aligned} r_{R3}^{suf} &= A_{suf}[k_{3,suf}^{+} C_{O_{2,suf}^{2-}} \frac{C_{V_O^{suf,n}}}{C_{O_{suf}^{2-}}^{max}} - k_{3,suf}^{-} \frac{(C_{O_{suf}^{-}})^2}{C_{O_{suf}^{2-}}^{max}}] \\ C_{V_O^{suf,n}} &= C_{V_O^{suf}} \exp(-\frac{G_{V_O^{suf,n}}(T) - G_{V_O^{suf}}(T)}{k_B T}) \end{aligned} \tag{3.12}$$

For reaction R4:

$$r_{R4}^{suf} = A_{suf}[k_{4_1,suf}^{+} C_{O_{suf}^{-}} \frac{C_{V_O^{sub_1}}}{C_{O_{suf}^{2-}}^{max}} - k_{4_1,suf}^{-} C_{O_{sub_1}^{2-}} \frac{C_{V_O^{suf}}}{C_{O_{suf}^{2-}}^{max}}] \tag{3.13}$$

For reaction R5:

$$\begin{aligned} r_{R5}^{int} &= A_{int}[k_{1,int}^{+} C_{V_O^{int_1}} \frac{C_{O^{2-}}}{C_{O_{suf}^{2-}}^{max}} - k_{1,int}^{-} C_{O_{int_1}^{2-}} \frac{C_{V_O}}{C_{O_{suf}^{2-}}^{max}}] \\ C_{V_O} &= C_{O^{2-}}^{max} - C_{O^{2-}} \end{aligned} \tag{3.14}$$

For reaction R6:

$$r_{R6}^{TPB} = A_{TPB}[k_{TPB}^{+} \exp(-\frac{F_a \eta}{RT}) C_{V_O^{ele}} \frac{C_{O_{2,suf}^{2-}}}{C_{O_{suf}^{2-}}^{max}} - k_{TPB}^{-} \exp(\frac{F_a \eta}{RT}) C_{O_{ele}^{-}} \frac{C_{O_{suf}^{-}}}{C_{O_{suf}^{2-}}^{max}}] \tag{3.15}$$

where A_{suf} denotes the LSCF surface area per unit volume, A_{int} denotes

the percentage of LSCF/GDC contacting surface area on the interface, A_{TPB} denotes the TPB length per unit interface area. Experimental values for A_{suf},A_{int},A_{TPB} are listed in Table 3.1. Additional details on obtaining $C_{V_O^{int_1}}$, $C_{O^{2-}_{int_1}}$, $C_{V_O^{sub_1}}$, $C_{O^{2-}_{sub_1}}$ are presented in Appendix B.

The expression for current density is given by:

$$I = 2F_a(-r_{R5}^{int} - r_{R6}^{TPB}) \tag{3.16}$$

The overall continuum model procedure is described in the flow chart in Figure 3.3. The coupled equations are numerically solved using the finite volume method in OpenFOAM[68] (Open Field Operation and Manipulation).

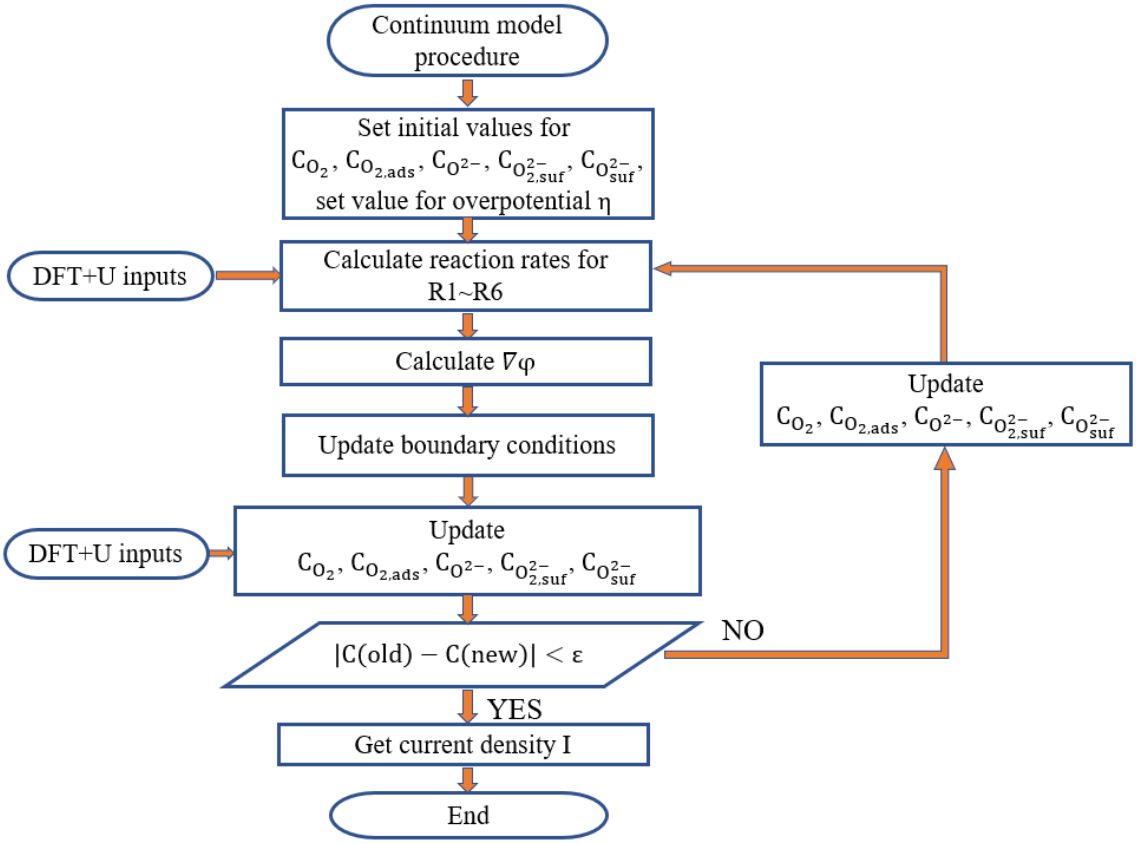

(a)

Figure 3.3: Flow chart of the overall continuum model procedure.

Table 3.1: LSCF electrode microstructural parameters. The values presented in the table are from literature [1].

A_{suf}	$5\mu m^2/\mu m^3$
A_{TPB}	$3.4\mu m/\mu m^2$
A_{int}	$0.6\mu m^2/\mu m^2$
ϕ_{gas}	0.4
ϕ_{LSCF}	0.6
τ_{gas}, τ_{LSCF}	1.46

3.3 Simulation Results

3.3.1 DFT+U Calculation Results

The DFT+U calculations contain three parts, the free energy profile calculations for LSCF surface reactions, the free energy profile calculations for LSCF/GDC interface reactions, and the free energy barrier calculations for LSCF surface oxide ion diffusions. The detailed energy barrier values are presented in Table 3.2 and Table 3.3. The optimized structures and additional details on these calculations are presented in Appendix C.

Figure 3.4(a) shows the free energy profile for the LSCF surface reactions, $O_2 + 4e^- + 2V_O \rightarrow 2O^{2-}$. The entire process includes 4 reactions, R1, R2, R3 and R4. R1 and R2 describe adsorption of O_2 on the LSCF surface and $O_{2,ads}$ occupying a vacancy on the surface, respectively. Our calculations suggest that these two steps are both endothermic. R3 describes the $O^{2-}_{2,suf}$ spliting process. From Figure 3.4(a) we see that it contains 2 sub steps. In the first sub step, V_O^{suf} transports to a neighboring positions of $O^{2-}_{2,suf}$, which is denoted as $V_O^{suf,n}$. Calculations reveal that the energy of the structure containing $V_O^{suf,n}$ is 1.465 eV higher than that containing V_O^{suf}. In the second sub step, $O^{2-}_{2,suf}$ splits into two O^-_{suf}. The energy barrier for $O^{2-}_{2,suf}$ split is 0.814 eV, and the barrier for combination of two O^-_{suf} is 2.343 eV. These high barriers indicate that this process can be a rate-limiting step. R4 describes the process of O^-_{suf} transports to the bulk LSCF. From the calculated results, we note that the oxide ions are less stable in the surface than in the bulk LSCF. This result is consistent with the literature, showing that surface vacancy segregation is an important phenomenon of LSCF[69]. It can be concluded that the largest barrier for the LSCF surface reactions comes from

step R3, which contains the oxygen-oxygen bond breaking in SOFC mode or bond forming in SOEC mode. Besides, the high energy of the $V_O^{suf,n}$-containing structure also slows down the overall reaction rates. It is observed from our relaxed structures that after $V_O^{suf,n}$ is introduced in the structure, the oxygen-oxygen bond length in $O_{2,suf}^{2-}$ stretches from $1.472\mathring{A}$ to $1.494\mathring{A}$, which means that $V_O^{suf,n}$ makes $O_{2,suf}^{2-}$ less stable and explains the relatively high energy of this structure.

Figure 3.4(b) shows the free energy profile for LSCF/GDC interface reaction R5, $O^{2-} + V_O^{ele} \rightarrow O_{ele}^{2-} + V_O$. This reaction contains 6 sub steps: the oxide ion migration from the bulk LSCF to the interfacial layers, migration within the interfacial layers and the migration from interfacial layers to the bulk electrolyte. Details on these sub steps and the definitions of layer indices are discussed in Appendix B. The free energy profile shows that oxygen vacancies are more stable in the interfacial layers than in bulk LSCF, and layer 5, the interfacial layer between SrO and CeO_2 layers, is the most stable layer for oxygen vacancies. The energy profile also shows that the largest barrier comes from the migration from layer 4 to layer 5 as well as from layer 5 to layer 6. Besides, it can be seen from Table 3.2 that the energy barriers at the interface are much smaller than that at the surface.

Figure 3.5 shows the free energy profile for diffusion of O_{suf}^{-} and $O_{2,suf}^{2-}$ at the LSCF surface. The free energy barrier for O_{suf}^{-} diffusion is very high, indicating that the diffusion of O_{suf}^{-} on the LSCF surface is very slow. The free energy barrier for $O_{2,suf}^{2-}$ diffusion (1.27 eV) is higher than that of the oxide ion diffusion in bulk LSCF (about 0.7 eV), and the calculated barrier is similar to the $O_{2,suf}^{2-}$ diffusion on other SrO terminated surfaces[25]. These results show that the SrO surface layer is inefficient for surface oxide ion diffusions.

3.3.2 Influence of Concentration Variation on Free Energy Barriers

Unlike $\Delta G(T)$, whose values are presented in Table 3.2, expressions for $\Delta G(C)$ are difficult to obtain theoretically. Therefore, we derived the $\Delta G(C)$ term for specific reaction steps based on the experimental observations available in the literature[31, 61, 32, 54].

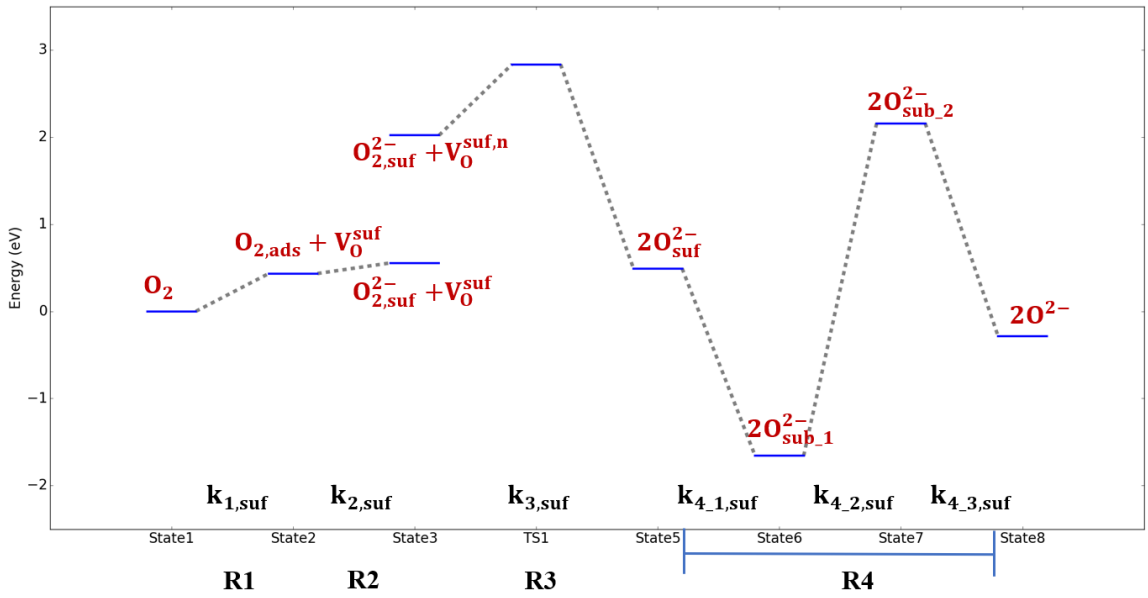

(a)

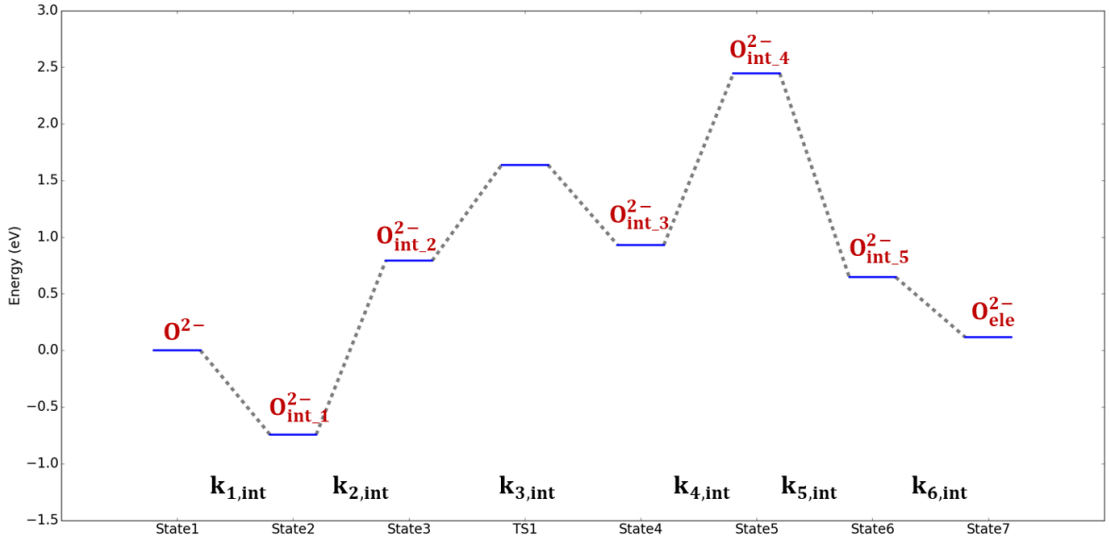

(b)

Figure 3.4: (a) Free energy profile for LSCF surface reactions. All energies are with reference to energies of the O_2 gas. This profile contains reactions R1, R2, R3 and R4. (b) Free energy profile for LSCF/GDC interface reactions R5. All energies are with reference to energies of the oxide ion in bulk LSCF.

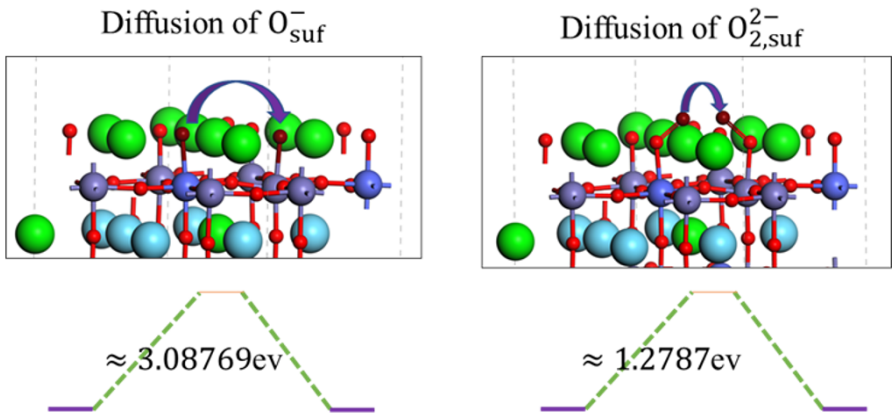

(a)

Figure 3.5: Free energy profile for ion diffusions on LSCF surface. The brown circles are the oxide ions that are moving in the process.

From reference [61], the vacancy formation energy of LSCF is related to the oxygen vacancy concentration:

$$\Delta G_{f,vac} = \Delta G^{perf}_{f,vac} + a\frac{C_{V_O}}{C^{max}_{O^{2-}}} \tag{3.17}$$

where $\Delta G_{f,vac}$ is the vacancy formation free energy, $\Delta G^{perf}_{f,vac}$ is the vacancy formation free energy with no vacancies in the lattice, and $'a'$ represents the deviation from the ideal structure. The interactions among defects and lattice ions account for the additional change in free energy[70, 71]. The experimental values for $'a'$ are presented in Table 3.4. Equation (3.17) implies that as C_{V_O} in bulk LSCF increases, the vacancies become less stable, and O^{2-} are more stable in the bulk. Stability of O^{2-} directly affects the reaction step R4 (accounts for the oxide ion migration between LSCF surface and bulk LSCF), and R5 (accounts for the oxide ion transport across the LSCF/GDC interface). Therefore, the reaction rate constants for $k^-_{4_3,suf}$,$k^+_{1,int}$ are modified as follows:

$$
\begin{aligned}
k^{-}_{4_3,suf} &= \frac{k_B T}{h}\exp(-\frac{\Delta G_{k^{-}_{4_3,suf}}(T)}{k_B T})\exp(-\frac{\Delta G_{k^{-}_{4_3,suf}}(C_{V_O})}{k_B T}) \\
k^{+}_{1,int} &= \frac{k_B T}{h}\exp(-\frac{\Delta G_{k^{+}_{1,int}}(T)}{k_B T})\exp(-\frac{\Delta G_{k^{+}_{1,int}}(C_{V_O})}{k_B T}) \\
\Delta G_{k^{-}_{4_3,suf}}(C_{V_O}) &= \Delta G_{k^{+}_{1,int}}(C_{V_O}) = a\frac{\Delta C_{V_O}}{C^{max}_{O^{2-}}}
\end{aligned}
\tag{3.18}
$$

From reference [54], bulk diffusivity and surface reaction rate constants of LSCF are all related to the pressure of oxygen gas. Thus, we have:

$$
\begin{aligned}
D_{O^{2-}} &= \frac{\lambda^2}{6}\frac{k_B T}{h}\exp(-\frac{\Delta G_{D_{O^{2-}}}(T)}{k_B T})\exp(-\frac{\Delta G_{D_{O^{2-}}}(C_{V_O})}{k_B T}) \\
\Delta G_{D_{O^{2-}}}(C_{V_O}) &= 2\gamma_{bulk} a\frac{\Delta C_{V_O}}{C^{max}_{O^{2-}}}
\end{aligned}
\tag{3.19}
$$

$$
\begin{aligned}
k^{+}_{3,suf} &= \frac{k_B T}{h}\exp(-\frac{\Delta G_{k^{+}_{3,suf}}(T)}{k_B T})\exp(-\frac{\Delta G_{k^{+}_{3,suf}}(C_{V_O})}{k_B T})\exp(-\frac{\Delta G_{k^{+}_{3,suf}}(C_{O^{-}_{suf}})}{k_B T}) \\
k^{-}_{3,suf} &= \frac{k_B T}{h}\exp(-\frac{\Delta G_{k^{-}_{3,suf}}(T)}{k_B T})\exp(-\frac{\Delta G_{k^{-}_{3,suf}}(C_{V_O})}{k_B T})\exp(-\frac{\Delta G_{k^{-}_{3,suf}}(C_{O^{-}_{suf}})}{k_B T}) \\
\Delta G_{k^{+}_{3,suf}}(C_{V_O}) &= \Delta G_{k^{-}_{3,suf}}(C_{V_O}) = 2\gamma_{suf} a\frac{\Delta C_{V_O}}{C^{max}_{O^{2-}}}
\end{aligned}
\tag{3.20}
$$

The experimental values for γ_{bulk},γ_{suf} are listed in Table 3.4. Details on the derivations of equations (3.19,3.20) are presented in Appendix A. Equations (3.19,3.20) imply that as C_{V_O} increases, O^{2-} are more stable, and their movements become more difficult. Such phenomenon can be explained based on Bader charge analysis. It is observed that after one vacancy is introduced into the bulk LSCF, the average Bader charge of O^{2-} changes from -1.231 to -1.264, and the average Bader charge of other cations increases slightly. This implies that vacancy introduction increases the electrostatic forces between cations and O^{2-} and results in an increase of the energy barrier.

As noted in references [31, 32], the electrostatic potential difference between the adsorbed oxygen layer and LSCF surface layer, which denotes χ, exists at the LSCF/gas interface, as shown in Figure 3.6. χ varies with overpotential. In the SOEC mode, O^{-}_{suf} enriches on the LSCF surface, and the

negative charge due to O^-_{suf} enrichment induces an increase of χ. In the SOFC mode, the positive charge due to the O^-_{suf} depletion induces the decrease of χ. The expressions for $\Delta G_{k^+_{3,suf}}(C_{O^-_{suf}})$, $\Delta G_{k^-_{3,suf}}(C_{O^-_{suf}})$ are given by:

$$\begin{aligned} \Delta G_{k^+_{3,suf}}(C_{O^-_{suf}}) &= \alpha e \Delta\chi \\ \Delta G_{k^-_{3,suf}}(C_{O^-_{suf}}) &= -(1-\alpha) e \Delta\chi \\ \Delta\chi &= \chi - \chi_{eqi} \end{aligned} \tag{3.21}$$

where e is the charge of an electron, α is the charge transfer coefficient, χ_{eqi} is the electrostatic potential step in equilibrium. As is shown in Figure 3.6(d), $\alpha = \frac{d_1}{d_1+d_2} \approx \frac{1}{3}$. The expression for χ is given by:

$$\begin{aligned} \chi &= \frac{F_a C_{O^-_{suf}}}{Cap_{suf}} \\ Cap_{suf} &= \frac{\varepsilon_{suf}}{d} \approx \frac{\varepsilon_{air} + \varepsilon_{LSCF}}{2d} \end{aligned} \tag{3.22}$$

where Cap_{suf} is the capacitance for surface LSCF, d is the vertical distance between the uppermost oxygen and the surface layer and is shown in Figure 3.6(c), and ε is the permittivity. Here we assume that the surface permittivity value ε_{suf} is the average of the air permittivity ε_{air} and the permittivity of LSCF/electrolyte interface ε_{LSCF}. This approximation is consistent with the parameters used in reference [72], showing that the capacitance at surface is approximately half the value of that at interface. The value for ε_{LSCF} is listed in Table 3.4.

$\Delta\chi$ helps lowering the reaction barriers. As is shown in Figure 3.6(a), in the SOEC mode (O^{2-} transfers from the electrolyte into LSCF), $C_{O^-_{suf}}$ is higher than in equilibrium, and the energy barrier for $k^-_{3,suf}$ becomes smaller, which makes the reaction faster. In the SOFC mode, $C_{O^-_{suf}}$ is lower than in equilibrium, and the energy barrier for $k^+_{3,suf}$ becomes smaller.

3.3.3 Continuum Modeling Results

The current density-overpotential plot is shown in Figure 3.7, and it is consistent with experimental results. Although the current density under SOEC mode is comparable to that under SOFC mode with the same overpotential

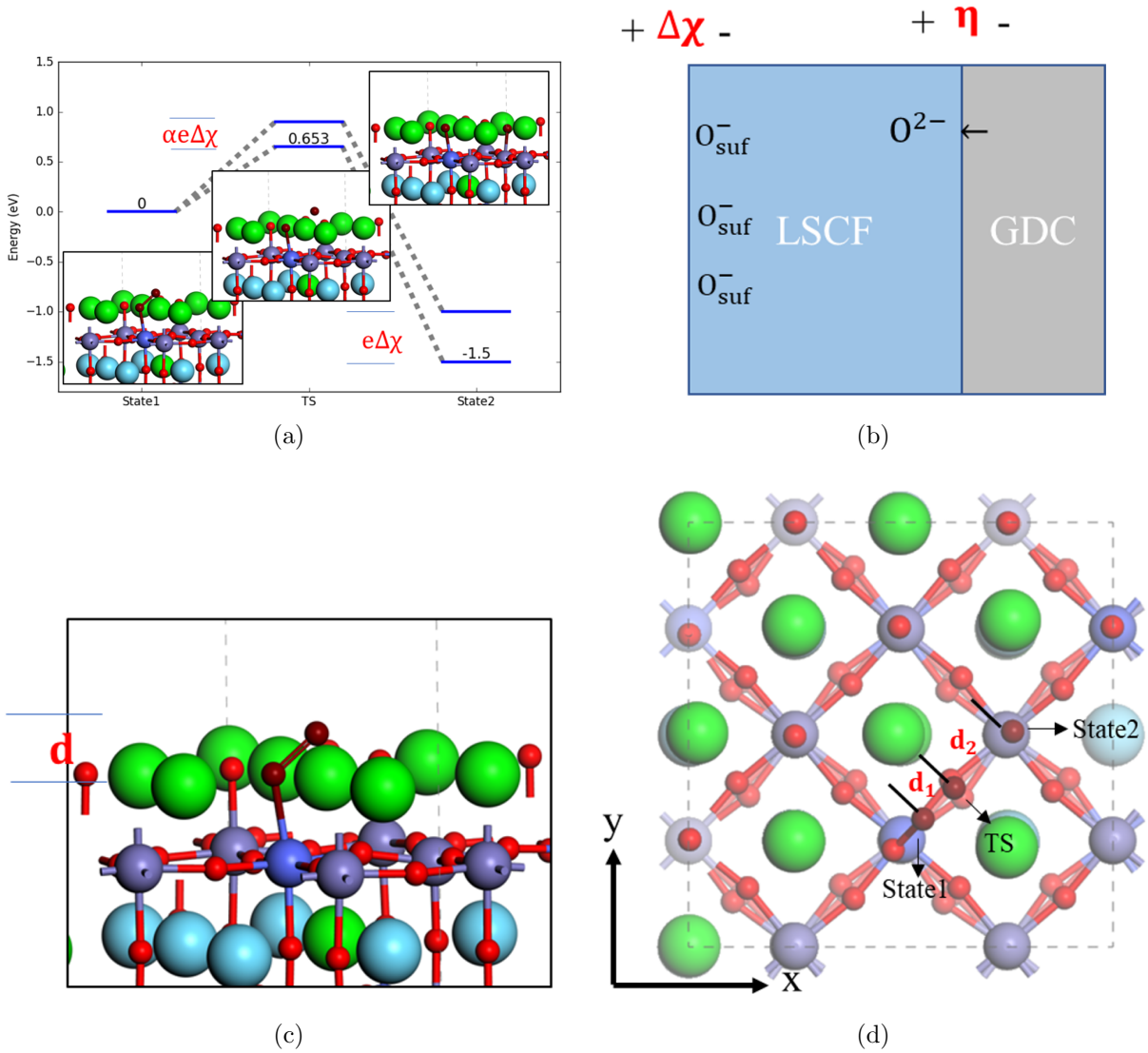

Figure 3.6: Schematic representation of the influence of electrostatic potential difference at the LSCF/gas interface on the reaction rate constants for R3. (a) The energy profile for R3 with and without the electrostatic potential step. (b) The mechanism of $\Delta\chi$ formation. When O^{2-} transfer from the electrolyte into LSCF, O^{-}_{suf} enrich at the LSCF surface, and induce the electric potential $\Delta\chi$. When O^{2-} transfer in reverse direction, $\Delta\chi$ will be negative. (c) Side view of LSCF surface with $O^{2-}_{2,suf}$. d is the vertical distance between the adsorbed oxygen layer and the surface layer. (d) Top view of the R3 process. Brown circles are the initial, transition and final state positions of the moving atom in the reaction. d_1,d_2 are the x-y plane distances of the moving atom between the initial and the transition state, and the transition and the final state, respectively.

magnitude, the governing mechanisms are different. It can be seen from Figure 3.8 that $D_{O^{2-}}$ under SOEC mode is much higher than that under SOFC mode, and C_{V_O} under SOEC mode is much lower than that under SOFC mode, which is consistent with the literature[21, 73]. Based on the current density expression $I = 2F_a(-D_{O^{2-}}\frac{d}{dz}C_{O^{2-}})$, I is limited by the low $\frac{d}{dz}C_{O^{2-}}$ in the SOEC mode, while I is limited by the low $D_{O^{2-}}$ in SOFC mode.

To analyze the importance of each parameter, sensitivity analysis was performed. The sensitivity of current density S_e to other parameters is given by:

$$S_e = \frac{\partial I/I}{\partial P_a/P_a} \approx \frac{\Delta I/I}{\Delta P_a/P_a} \tag{3.23}$$

where P_a is the parameter of interest. As shown in Table 3.5 that, the current density is sensitive to the reaction rate constants for R3, $k^+_{3,suf}$ and $k^-_{3,suf}$, and the oxide ion diffusivity $D_{O^{2-}}$. Therefore, it can be concluded that reaction step R3, the oxygen-oxygen bond breaking and forming step in SOFC/SOEC, respectively, and O^{2-} diffusion in bulk LSCF are the two essential steps for the system, and improving $k^+_{3,suf}$,$k^-_{3,suf}$ and $D_{O^{2-}}$ can greatly enhance the current density.

In addition, neglecting of the reaction path across the TPB is a valid assumption. It can be seen from Table 3.3 and Figure 3.5 that the surface diffusivities of O^-_{suf} and $O^{2-}_{2,suf}$ are both much lower compared to bulk O^{2-} diffusivity. The low surface diffusivities make the contribution of the reaction path B shown in Figure 3.1 insignificant. It is found that when the concentrations of different species are all within the physical limits:

$$\begin{aligned} 0 \leq C_{O^{2-}_{suf}}, C_{O^{2-}_{2,suf}}, C_{O_{2,ads}} \leq C^{max}_{O^{2-}_{suf}} \\ 0 \leq C_{O^{2-}} \leq C^{max}_{O^{2-}} \end{aligned} \tag{3.24}$$

We have

$$I_{TPB} = -2F_a r^{TPB}_{R6} \leq 0.03 A cm^{-2} \tag{3.25}$$

where I_{TPB} is the current density across the three-phase boundary, and its value is much smaller than the experimental current density. Therefore, this reaction path is neglected in this work.

Low I_{TPB} is attributed to two reasons. First, due to the low surface

diffusivities of $O^{2-}_{2,suf}$ and O^{2-}_{suf}, $O^{2-}_{2,suf}$ and O^{2-}_{suf} far away from the TPB find it difficult to transport to the TPB. Therefore, only the O_2 molecules near the TPB can be incorporated into the electrolyte through path B, and this makes the reaction rate from this path very slow. On the contrary, once oxide ions transport into the bulk LSCF, they can diffuse fast in bulk LSCF. Therefore, the O_2 molecules far from the LSCF/GDC interface can be easily incorporated into the bulk LSCF, then transport across the LSCF/GDC interface and into the electrolyte. This makes the reaction rate from path A in Figure 3.1 much faster than path B and I_{int} much larger than I_{TPB}. Second, the electrode structure here is the LSCF single-phase electrode. As shown in Figure 3.1, TPB only exists at the bottom of the electrode, and the small TPB surface area contributes to the low I_{TPB}. As for other electrode structures, such as LSCF-CGO composite electrode[1], TPB can exist in bulk electrode and I_{TPB} can be higher.

Based on the above analysis, SrO terminated LSCF surface is not an efficient surface structure for oxygen oxidation and reduction reactions. On the one hand, $C_{O^{2-}_{2,suf}}$ and $C_{O^{2-}_{suf}}$ diffuse very slowly on SrO terminated surface. It can be seen from equation (3.25) that, the slow surface diffusions make I_{TPB} very small. On the other hand, the high energy barrier for reaction step R3 from DFT+U calculations result in the slow reaction rate, indicating that SrO terminated surface is not a good catalyst for the splitting of $O^{2-}_{2,suf}$ or combination of two O^{-}_{suf}. Such phenomenon is also discussed in recently published experimental work[74].

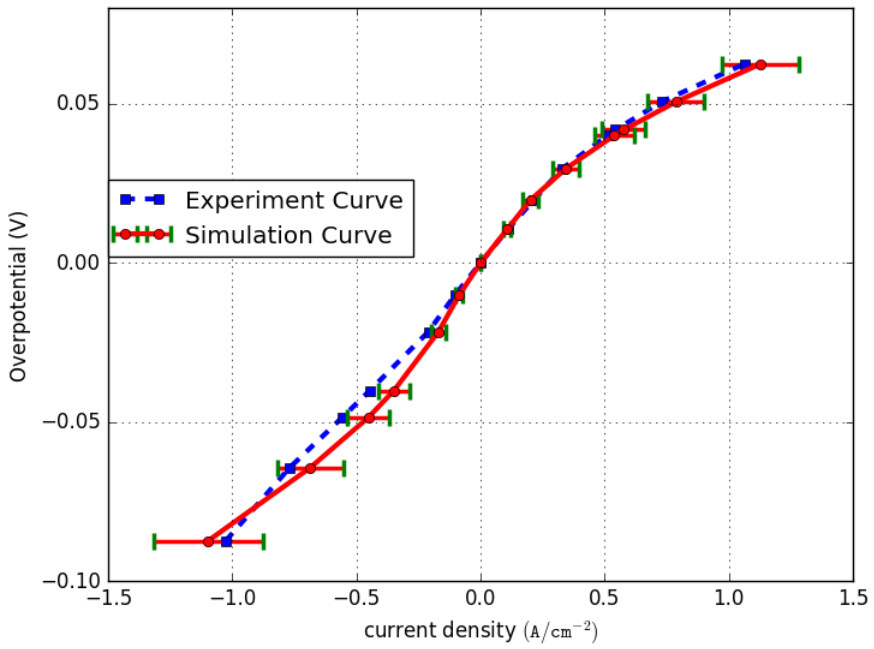

(a)

Figure 3.7: Simulation and experimental LSCF based electrode overpotential-current density curve under pressure = 1atm and temperature = 1073K. When current density is less than 0, the cell is working under fuel cell mode; when current density is larger than 0, the cell is working under electrolysis cell mode. Error bars on the simulation curve come from the uncertainties from published experimental parameters.

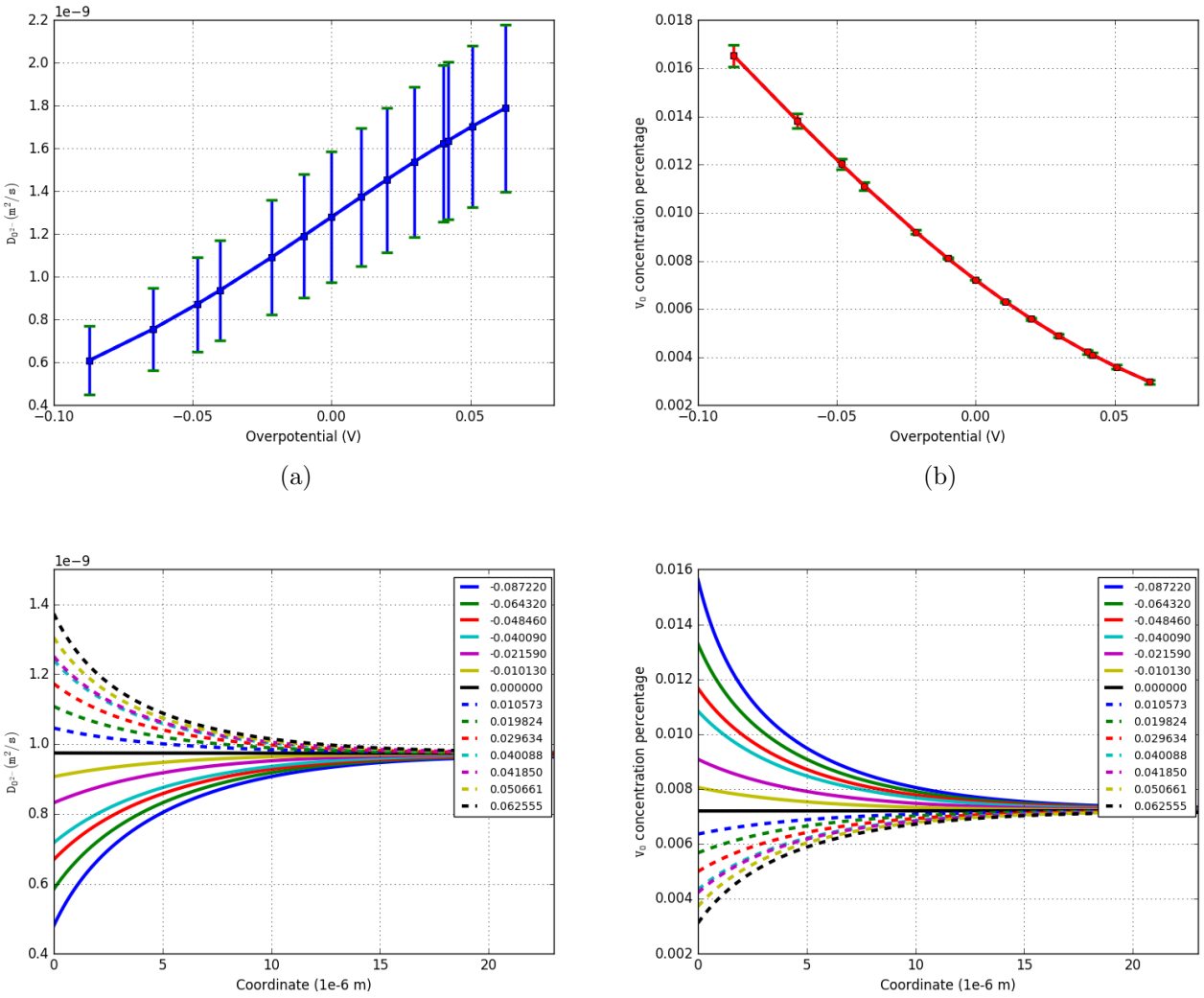

Figure 3.8: (a) $D_{O^{2-}}$ at LSCF/GDC interface as a function of overpotential. (b) Vacancy concentration percentage at LSCF/GDC interface as a function of overpotential. (c) $D_{O^{2-}}$ as a function of z-axis coordinate. Different lines represent different overpotential values, ranging from -0.08722 Volt to 0.062555 Volt. (d) Vacancy concentration percentage in bulk LSCF as a function of z-axis coordinate. Different lines represent different overpotential values.

Table 3.2: Internal energy barriers and free energy barriers for each reaction rate constant. Here $\Delta G(T)$ is the free energy barrier at temperature T=1073K.

Parameters	Δ G(T)(eV)	Values (s^{-1})
$k^{+}_{1,suf}$	0.4337	2.06198×10^{11}
$k^{-}_{1,suf}$	0	2.2347×10^{13}
$k^{+}_{2,suf}$	0.1214	6.06167×10^{12}
$k^{-}_{2,suf}$	0	2.2347×10^{13}
$k^{+}_{3,suf}$	0.8138	3.3939×10^{9}
$k^{-}_{3,suf}$	2.3432	2.2664×10^{2}
$k^{+}_{4_1,suf}$	0	2.2347×10^{13}
$k^{-}_{4_1,suf}$	1.07428	2.03546×10^{8}
$k^{+}_{4_2,suf}$	1.9076	2.5033×10^{4}
$k^{-}_{4_2,suf}$	0	2.2347×10^{13}
$k^{+}_{4_3,suf}$	0	2.2347×10^{13}
$k^{-}_{4_3,suf}$	1.2838	2.116×10^{7}
$k^{+}_{1,int}$	0	2.2347×10^{13}
$k^{-}_{1,int}$	0.6807	1.43×10^{10}
$k^{+}_{2,int}$	1.53418	1.4151×10^{6}
$k^{-}_{2,int}$	0	2.2347×10^{13}
$k^{+}_{3,int}$	0.8457	2.406×10^{9}
$k^{-}_{3,int}$	0.706	1.088×10^{10}
$k^{+}_{4,int}$	1.5138	1.7635×10^{6}
$k^{-}_{4,int}$	0	2.2347×10^{13}
$k^{+}_{5,int}$	0	2.2347×10^{13}
$k^{-}_{5,int}$	1.7985	8.1395×10^{4}
$k^{+}_{6,int}$	0	2.2347×10^{13}
$k^{-}_{6,int}$	0.5297	7.3046×10^{10}

Table 3.3: Internal energy barriers and free energy barriers for diffusivities. Here λ is the migration length. The value for $D_{O^{2-}}$ is from experiments, and the value for D_{O_2} is from Dusty Gas Model[1].

Parameters	Δ G(T)(eV)	$\lambda \mathring{A}$	Values (s^{-1})
$D_{O^{2-}}$[53, 54]	/	/	[9.73,15.85]$\times 10^{-10}$
D_{O_2}[1]	/	/	1.2×10^{-5}
$D_{O_{2,ads}}$	0	3.843	8.25×10^{-7}
$D_{O^{2-}_{2,ads}}$	1.2787	1.9215	2.0639×10^{-13}
$D_{O^{2-}_{suf}}$	3.08769	3.843	2.6851×10^{-21}

Table 3.4: Parameters used in $\Delta G(C)$ expressions.

Parameters	Experimental Values
a[61]	[9.2,10.86]eV
γ_{bulk}[54]	0.37
γ_{suf}[54]	0.56
ε_{LSCF}[75, 76]	11.068

Table 3.5: Sensitivity analysis results of the parameters.

Parameters	$\Delta P_a/P_a$	$S_e(\eta = -0.08722V)$	$S_e(\eta = -0.062555V)$
$k^+_{1,suf}, k^-_{1,suf}$	0.05	≈ 0	≈ 0
$k^+_{2,suf}, k^-_{2,suf}$	0.05	≈ 0	≈ 0
$k^+_{3,suf}, k^-_{3,suf}$	0.05	[0.466,0.477]	[0.460,0.476]
$k^+_{4,suf}, k^-_{4,suf}$	0.05	[0.0091,0.0136]	[0.00225,0.0344]
k^+_{int}, k^-_{int}	0.05	[0.0272,0.0334]	[0.00225,0.00939]
$D_{O^{2-}}$	0.05	[0.467,0.482]	[0.477,0.481]
$D_{O_{2,ads}}$	0.05	≈ 0	≈ 0
$D_{O^{2-}_{2,suf}}$	0.05	≈ 0	≈ 0
$D_{O^{2-}_{suf}}$	0.05	≈ 0	≈ 0

CHAPTER 4

MODELING OF PROTON-CONDUCTING SOLID OXIDE FUEL CELL

In this chapter, we develop a multiscale approach combining DFT-based quantum scale simulations, transition state theory and continuum scale simulations to determine the key reaction steps in the Pt/Y-doped BaZrO3/Ag based proton-conducting SOFC. First, DFT calculations are performed to calculate the energy barriers for each reaction step and the vibrational frequencies of atoms, to obtain the free energy landscape of the entire reaction processes. These results are used in the transition state theory to obtain the reaction rate constants and diffusivities. These results are subsequently used in the continuum theory to calculate the current density-voltage loss curves which are compared with the experimental data.

4.1 Model Structure and Reaction Steps

The overall structure modeled in this paper is the same as that in reference [2] and shown in Figure 4.1. The anode is made of porous Pt, the cathode is made of porous Ag, and the electrolyte is made of Y-doped $BaZrO_3$. The anode and the cathode atmospheres are wet (7.3 kPa) H_2 and wet (2.3 kPa) air. All the reactions are at 873K, which is the same temperature as in experiments. The reactions happened in the cell are shown in Figure 4.1. The entire reaction process can be separated into 13 transport steps (T1 to T13) and 11 reaction steps (R1 to R11) and are presented below:

The 13 transport steps:

1. Transport of H_2 in gas phase (T1).
2. Transport of O_2 in gas phase (T2).
3. Transport of H_2O in gas phase (T3).

4. Transport of $H_{2,Pt}$ on Pt surface (T4).
5. Transport of $O_{2,Ag}$ on Ag surface (T5).
6. Transport of H_2O_{Ag} on Ag surface (T6).
7. Transport of H^+ on Pt surface (T7).
8. Transport of H^+ on Ag surface (T8).
9. Transport of O^{2-} on Ag surface (T9).
10. Transport of OH^- on Ag surface (T10).
11. Transport of H^+ in bulk electrolyte (T11).
12. Transport of e^- in Pt (T12).
13. Transport of e^- in Ag (T13).

where $H_{2,Pt}$ denotes the adsorbed H_2 on Pt surface, $O_{2,Ag}$ denotes the adsorbed O_2 on Ag surface, H_2O_{Ag} denotes the adsorbed H_2O on Ag surface. The 11 reaction steps:

1. Adsorption of H_2 on Pt surface (R1):

$$\mathrm{H_2} \longrightarrow \mathrm{H_{2,Pt}}$$

2. $H_{2,Pt}$ splits into 2 H^+ on Pt surface (R2):

$$\mathrm{H_{2,Pt}} \longrightarrow 2\mathrm{H^+_{Pt}} + 2\mathrm{e^-}$$

3. H^+ transports across the Pt-BZY-air TPB (R3):

$$\mathrm{H^+_{Pt}} \longrightarrow \mathrm{H^+_{BZY}}$$

4. H^+ transports across the Ag-BZY-air TPB (R4):

$$\mathrm{H^+_{BZY}} \longrightarrow \mathrm{H^+_{Ag}}$$

5. H^+ transports across the Ag-BZY-air TPB and react with O^{2-} on Ag surface (R5):

$$\mathrm{H^+_{BZY}} + \mathrm{O^{2-}_{Ag}} \rightarrow \mathrm{OH^-_{Ag}}$$

6. H^+ transports across the Ag-BZY-air TPB and react with OH^- on Ag surface (R6):

$$\mathrm{H^+_{BZY}} + \mathrm{OH^{2-}_{Ag}} \rightarrow \mathrm{H_2O_{Ag}}$$

7. Adsorption of O_2 on Ag surface (R7):

$$\mathrm{O_2} \rightarrow \mathrm{O_{2,Ag}}$$

8. $O_{2,Ag}$ splits into 2 O^{2-} on Ag surface (R8):

$$\mathrm{O_{2,Ag}} + 4\mathrm{e^-} \rightarrow 2\mathrm{O^{2-}_{Ag}}$$

9. Combination of H^+ and O^{2-} into OH^- on Ag surface (R9):

$$\mathrm{H^+_{Ag}} + \mathrm{O^{2-}_{Ag}} \rightarrow \mathrm{OH^-_{Ag}}$$

10. Combination of H^+ and OH^- into H_2O adsorbed on Ag surface (R10):

$$\mathrm{H^+_{Ag}} + \mathrm{OH^-_{Ag}} \rightarrow \mathrm{H_2O_{Ag}}$$

11. Desorption of H_2O_{Ag} from Ag surface (R11):

$$\mathrm{H_2O_{Ag}} \rightarrow \mathrm{H_2O}$$

where H^+_{Pt} denotes the H^+ on Pt surface, H^+_{BZY} denotes the H^+ in bulk BZY, H^+_{Ag} denotes the H^+ on Ag surface, OH^-_{Ag} denotes the OH^- on Ag surface, O^{2-}_{Ag} denotes the O^{2-} on Ag surface.

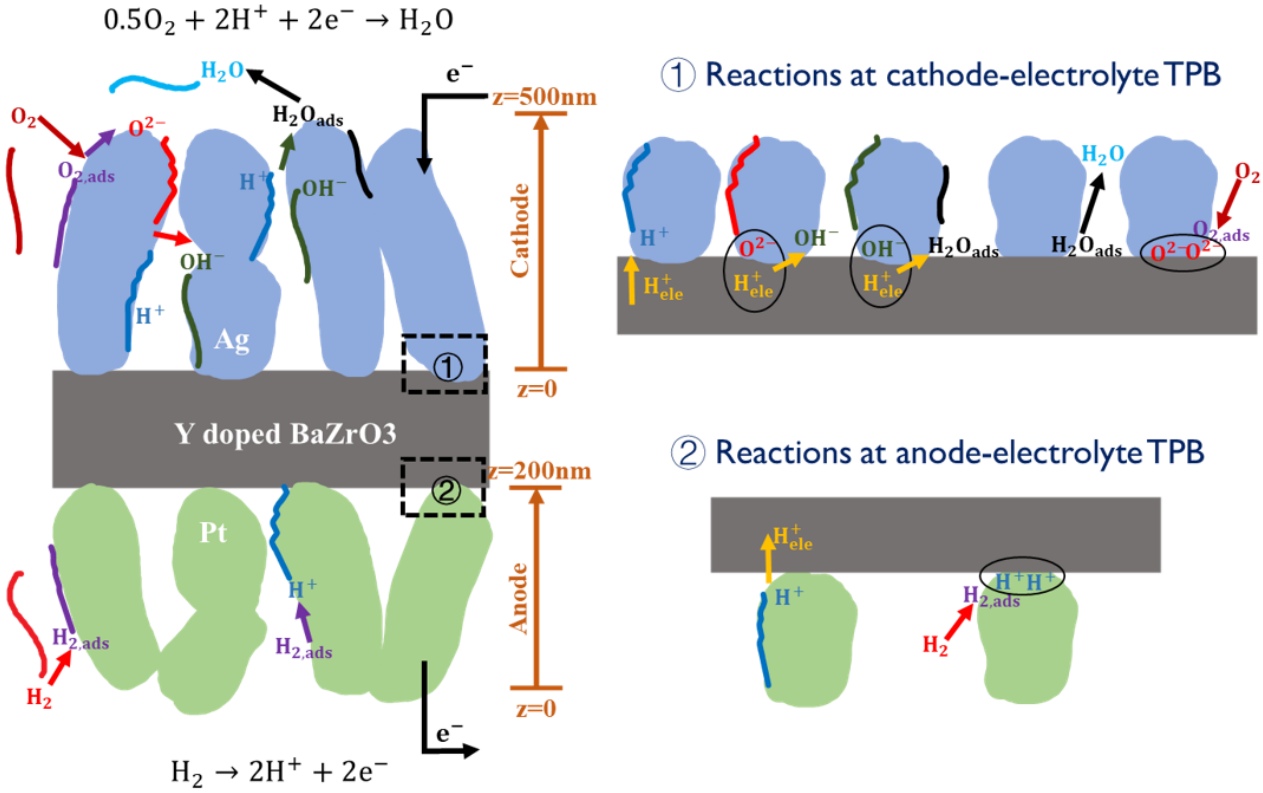

Figure 4.1: Schematic representation of the reactive pathways for Pt/BZY/Ag based proton-conducting SOFC. The blue grains are the Ag phase, the green grains are the Pt phase, the white spaces between them are the gas phase, and the gray rectangle is the electrolyte. The left graph shows the reactions that happen on the surface of electrodes, and the right graphs show the reactions that happen on the TPB.

4.2 Simulation Details

4.2.1 DFT Calculations

It can be seen from the reaction steps and the transport steps above that, the reaction and transport processes happen on metal (Ag, Pt) surfaces, in the bulk BZY as well as across the metal-BZY-air TPB. Because the diffusion of proton in the bulk BZY is well-explained in the literature[34, 77, 78, 79], here we did not perform the DFT calculations for this process.

To study the reactions on the metal surfaces, here the (111) oriented Pt surface slab and the (111) oriented Ag surface slab were constructed, which are shown in Figure 4.2(a-b). A vacuum slab larger than $15\mathring{A}$ was used above the surface to minimize the interactions between the surface structure and its periodic images. The bottom layer atoms were fixed at the bulk position, while the rest of the atoms were fully relaxed.

The TPB structure used in the calculations is shown in Figure 4.2(c-d). Here we used a (001) oriented 4-layer slab for the BZY phase. To simulate the complex TPB structure, a 10-atom metal cluster was constructed at the surface of BZY, which is the same as reference [80]. Although it is a simplified TPB structure, it can help us understand the reaction mechanisms around the TPB. A vacuum slab larger than $15\mathring{A}$ was used to minimize the interactions between the TPB structure and its images. The bottom layer atoms were fixed at the bulk position, while the rest of the atoms were fully relaxed.

4.2.2 Continuum Modeling

The entire reduction process is separated into 13 transport steps and 11 reaction steps, as stated above. Here a 1-D continuum model is used to describe them. They are presented as follows:

In the anode(Pt) domain, 4 transport equations will be solved:

Transport of H_2 in gas phase (T1):

$$\frac{d}{dz}(-\frac{\phi_{gas}}{\tau_{gas}}D_{H_2}\frac{d}{dz}C_{H_2}) = -r_{R1} \tag{4.1}$$

Transport of $H_{2,Pt}$ on Pt surface (T4):

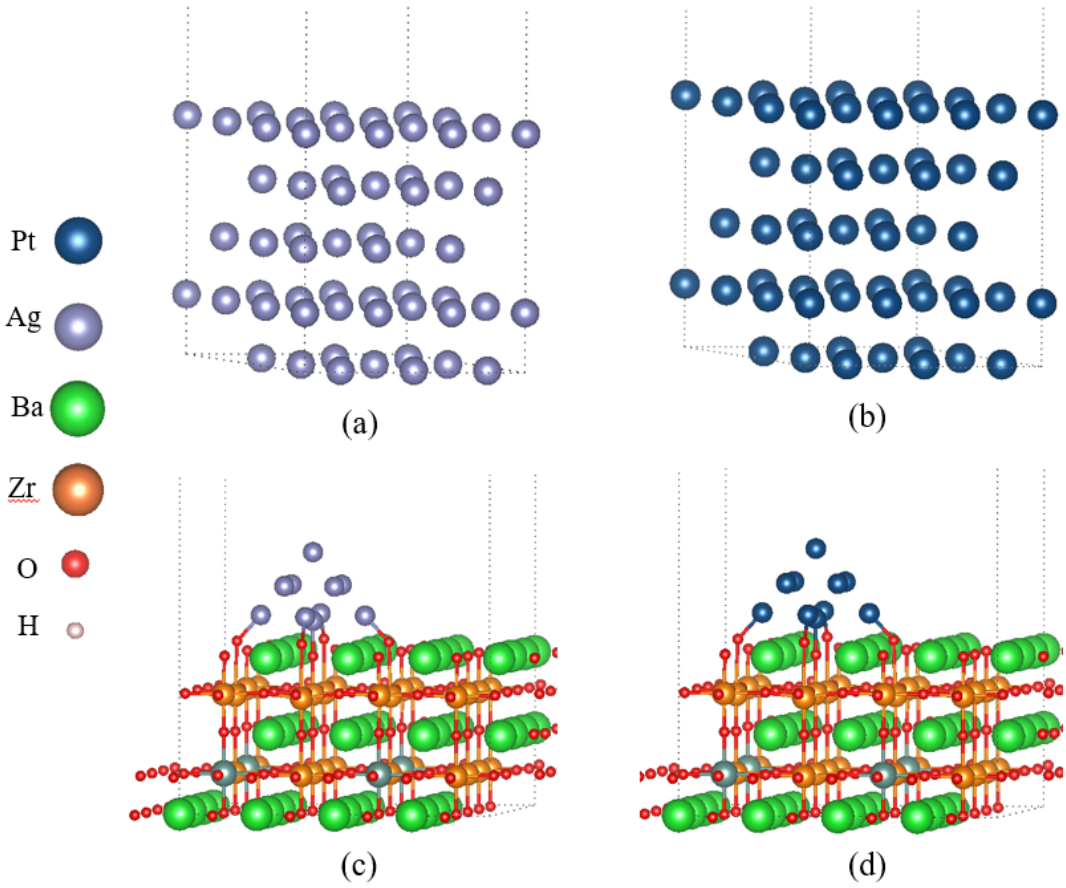

(a)

Figure 4.2: The structures used in the DFT calculations. The structures shown in the figures are after structural relaxations. (a-b) Side view of the metal surface structure. (c-d) Side view of the metal-BZY-air TPB structure.

$$\frac{d}{dz}(-\frac{\phi_{Pt}}{\tau_{Pt}}D_{H_{2,Pt}}\frac{d}{dz}C_{H_{2,Pt}}) = r_{R1} - r_{R2} \tag{4.2}$$

Transport of H^+ on Pt surface (T7):

$$\frac{d}{dz}[-\frac{\phi_{Pt}}{\tau_{Pt}}D_{H^+_{Pt}}(\frac{d}{dz}C_{H^+_{Pt}} + \frac{F_a C_{H^+_{Pt}}}{RT}\frac{d}{dz}\varphi)] = r_{R3} \tag{4.3}$$

Transport of e^- in Pt (T12):

$$\frac{d}{dz}[-\frac{\phi_{Pt}}{\tau_{Pt}}D_{e^-}(\frac{d}{dz}C_{e^-} - \frac{F_a C_{e^-}}{RT}\frac{d}{dz}\varphi)] = 0 \tag{4.4}$$

In the electrolyte(BZY) domain, 1 transport equation will be solved:
Transport of H^+ in bulk electrolyte (T11):

$$\frac{d}{dz}[-D_{H^+_{BZY}}(\frac{d}{dz}C_{H^+_{BZY}} + \frac{F_a C_{H^+_{BZY}}}{RT}\frac{d}{dz}\varphi)] = 0 \tag{4.5}$$

In the cathode(Ag) domain, 8 transport equations will be solved:
Transport of O_2 in gas phase (T2):

$$\frac{d}{dz}(-\frac{\phi_{gas}}{\tau_{gas}}D_{O_2}\frac{d}{dz}C_{O_2}) = -r_{R7} \tag{4.6}$$

Transport of H_2O in gas phase (T3):

$$\frac{d}{dz}(-\frac{\phi_{gas}}{\tau_{gas}}D_{H_2O}\frac{d}{dz}C_{H_2O}) = r_{R11} \tag{4.7}$$

Transport of $O_{2,Ag}$ on Ag surface (T5):

$$\frac{d}{dz}(-\frac{\phi_{Ag}}{\tau_{Ag}}D_{O_{2,Ag}}\frac{d}{dz}C_{O_{2,Ag}}) = r_{R7} \tag{4.8}$$

Transport of H_2O_{Ag} on Ag surface (T6):

$$\frac{d}{dz}(-\frac{\phi_{Ag}}{\tau_{Ag}}D_{H_2O_{Ag}}\frac{d}{dz}C_{H_2O_{Ag}}) = r_{R10} - r_{R11} \tag{4.9}$$

Transport of H^+ on Ag surface (T8):

$$\frac{d}{dz}[-\frac{\phi_{Ag}}{\tau_{Ag}}D_{H^+_{Ag}}(\frac{d}{dz}C_{H^+_{Ag}} + \frac{F_a C_{H^+_{Ag}}}{RT}\frac{d}{dz}\varphi)] = -r_{R9} - r_{R10} \tag{4.10}$$

Transport of O^{2-} on Ag surface (T9):

$$\frac{d}{dz}[-\frac{\phi_{Ag}}{\tau_{Ag}}D_{O^{2-}_{Ag}}(\frac{d}{dz}C_{O^{2-}_{Ag}}-\frac{2F_aC_{O^{2-}_{Ag}}}{RT}\frac{d}{dz}\varphi)]=2r_{R8}-r_{R9} \tag{4.11}$$

Transport of OH^- on Ag surface (T10):

$$\frac{d}{dz}[-\frac{\phi_{Ag}}{\tau_{Ag}}D_{OH^-_{Ag}}(\frac{d}{dz}C_{OH^-_{Ag}}-\frac{F_aC_{OH^-_{Ag}}}{RT}\frac{d}{dz}\varphi)]=r_{R9}-r_{R10} \tag{4.12}$$

Transport of e^- in Ag (T13):

$$\frac{d}{dz}[-\frac{\phi_{Ag}}{\tau_{Ag}}D_{e^-}(\frac{d}{dz}C_{e^-}-\frac{F_aC_{e^-}}{RT}\frac{d}{dz}\varphi)]=0 \tag{4.13}$$

Experimental values for ϕ_{gas},τ_{gas},ϕ_{Ag},τ_{Ag},ϕ_{Pt},τ_{Pt} are in Table 4.1. The potential distribution is solved using Poisson equation:

$$\frac{d^2}{dz^2}\varphi=\frac{-\rho}{\epsilon_0\epsilon_r} \tag{4.14}$$

The distribution of the relative permittivity ϵ_r is shown in Figure 4.3.

As is shown in Figure 4.1, the boundary conditions are as follows:

At the bottom of the overall cell:

$$\begin{aligned}\varphi &= V_0\\ C_{H_2} &= Const\\ \frac{d}{dz}C_i=0, i &= H_{2,Pt}, H^+_{Pt}, e^-\end{aligned} \tag{4.15}$$

At the Pt/BZY/air TPB:

$$\begin{aligned}-\frac{\phi_{Pt}}{\tau_{Pt}}D_{H^+_{Pt}}(\frac{d}{dz}C_{H^+_{Pt}}+\frac{F_aC_{H^+_{Pt}}}{RT}\frac{d}{dz}\varphi)&=-r_{R3}\\ -D_{H^+_{BZY}}(\frac{d}{dz}C_{H^+_{BZY}}+\frac{F_aC_{H^+_{BZY}}}{RT}\frac{d}{dz}\varphi)&=r_{R3}\\ \frac{d}{dz}C_i=0, i &= H_2, H_{2,Pt}, e^-\end{aligned} \tag{4.16}$$

At the Ag/BZY/air TPB:

$$\begin{aligned}
-\frac{\phi_{Ag}}{\tau_{Ag}} D_{H^+_{Ag}} (\frac{d}{dz} C_{H^+_{Ag}} + \frac{F_a C_{H^+_{Ag}}}{RT} \frac{d}{dz}\varphi) &= r_{R4} \\
-D_{H^+_{BZY}} (\frac{d}{dz} C_{H^+_{BZY}} + \frac{F_a C_{H^+_{BZY}}}{RT} \frac{d}{dz}\varphi) &= -r_{R4} \\
-\frac{\phi_{Ag}}{\tau_{Ag}} D_{O^{2-}_{Ag}} (\frac{d}{dz} C_{O^{2-}_{Ag}} - \frac{2F_a C_{H^+_{Ag}}}{RT} \frac{d}{dz}\varphi) &= -r_{R5} \\
-\frac{\phi_{Ag}}{\tau_{Ag}} D_{OH^-_{Ag}} (\frac{d}{dz} C_{OH^-_{Ag}} - \frac{F_a C_{OH^-_{Ag}}}{RT} \frac{d}{dz}\varphi) &= -r_{R6} \\
\frac{d}{dz} C_i = 0, i = O_{2,Ag}, H_2O_{Ag}, H_2O, O_2, e^-
\end{aligned} \tag{4.17}$$

At the top of the overall cell:

$$\begin{aligned}
\varphi &= V_1 \\
C_i &= Const, i = H_2O, O_2 \\
\frac{d}{dz} C_i = 0, i &= O_{2,Ag}, H_2O_{Ag}, O^{2-}_{Ag}, H^+_{Ag}, OH^-_{Ag}, e^-
\end{aligned} \tag{4.18}$$

The reaction rate expressions for R1-R11 are as follows:
For reaction R1:

$$r_{R1} = A_{Pt}[k_1^+ C_{H_2} - k_1^- C_{H_{2,Pt}}] \tag{4.19}$$

For reaction R2:

$$r_{R2} = A_{Pt}[k_2^+ C_{H_{2,Pt}} - k_2^- \frac{(C_{H^+_{Pt}})^2}{C^{max}_{H^+_{Pt}}}] \tag{4.20}$$

For reaction R3:

$$r_{R3} = A_{Pt-TPB}[k_3^+ \exp(-\frac{\alpha_A F_a \eta_A}{RT}) C_{H^+_{Pt}} - k_3^- \exp(\frac{(1-\alpha_A) F_a \eta_A}{RT}) C_{H^+_{BZY}}] \tag{4.21}$$

For reaction R4:

$$r_{R4} = A_{Ag-TPB}[k_4^+ \exp(-\frac{\alpha_C F_a \eta_C}{RT}) C_{H^+_{BZY}} - k_4^- \exp(\frac{(1-\alpha_C) F_a \eta_C}{RT}) C_{H^+_{Ag}}] \tag{4.22}$$

For reaction R5:

$$r_{R5} = A_{Ag-TPB}[k_5^+ \exp(-\frac{\alpha_C F_a \eta_C}{RT}) C_{O_{Ag}^{2-}} \frac{C_{H_{BZY}^+}}{C_{H_{BZY}^+}^{max}} - k_5^- \exp(\frac{(1-\alpha_C) F_a \eta_C}{RT}) C_{OH_{Ag}^-}] \tag{4.23}$$

For reaction R6:

$$r_{R6} = A_{Ag-TPB}[k_6^+ \exp(-\frac{\alpha_C F_a \eta_C}{RT}) C_{OH_{Ag}^-} \frac{C_{H_{BZY}^+}}{C_{H_{BZY}^+}^{max}} - k_6^- \exp(\frac{(1-\alpha_C) F_a \eta_C}{RT}) C_{H_2O_{Ag}}] \tag{4.24}$$

For reaction R7:

$$r_{R7} = A_{Ag}[k_7^+ C_{O_2} - k_7^- C_{O_{2,Ag}}] \tag{4.25}$$

For reaction R8:

$$r_{R8} = A_{Ag}[k_8^+ C_{O_{2,Pt}} - k_8^- \frac{(C_{O_{Pt}^+})^2}{C_{O_{Pt}^+}^{max}}] \tag{4.26}$$

For reaction R9:

$$r_{R9} = A_{Ag}[k_9^+ C_{O_{Ag}^{2-}} \frac{C_{H_{Ag}^+}}{C_{H_{Ag}^+}^{max}} - k_9^- C_{OH_{Ag}^-}] \tag{4.27}$$

For reaction R10:

$$r_{R10} = A_{Ag}[k_{10}^+ C_{OH_{Ag}^-} \frac{C_{H_{Ag}^+}}{C_{H_{Ag}^+}^{max}} - k_{10}^- C_{H_2O_{Ag}}] \tag{4.28}$$

For reaction R11:

$$r_{R11} = A_{Ag}[k_{11}^+ C_{H_2O_{Ag}} - k_{11}^- C_{H_2O}] \tag{4.29}$$

where A_{Pt} denotes Pt surface area per unit volume, A_{Ag} denotes Ag surface area per unit volume, A_{Pt-TPB} denotes Pt/BZY/air TPB length per unit interface area, A_{Ag-TPB} denotes Ag/BZY/air TPB length per unit interface area, α_A,α_C denotes the anode and cathode charge transfer coefficient, respectively, η_A denotes the anode overpotential, η_C denotes the cathode overpotential. The expressions for η_A, η_C are as follows:

Table 4.1: Electrode microstructural parameters for the proton-conducting system. The values presented in the table are extracted from the microstructure figures presented in literature [2].

A_{Pt},A_{Ag}	$5\mu m^2/\mu m^3$
A_{Ag-TPB}	$2.9\mu m/\mu m^2$
A_{Pt-TPB}	$3.45\mu m^2/\mu m^2$
ϕ_{gas}	0.4
ϕ_{Pt}, ϕ_{Ag}	0.6
$\tau_{gas}, \tau_{Pt}, \tau_{Ag}$	1.46

$$\begin{aligned} \eta_A &= \varphi_A^+ - \varphi_A^- \\ \eta_C &= \varphi_C^+ - \varphi_C^- \end{aligned} \tag{4.30}$$

The positions for $\varphi_A^+, \varphi_A^-, \varphi_C^+, \varphi_C^-$ are presented in Figure 4.3.

Experimental values for A_{Pt}, A_{Ag}, A_{Pt-TPB}, A_{Ag-TPB} are listed in Table 4.1. The expression for current density is given by:

$$\begin{aligned} I_A &= F_a r_{R3} \\ I_C &= F_a(r_{R4} + r_{R5} + r_{R6}) \end{aligned} \tag{4.31}$$

where I_A denotes the current density at the anode/electrolyte interface, I_C denotes the current density at the cathode/electrolyte interface. The overall continuum model procedure is described in the flow chart in Figure 4.4.

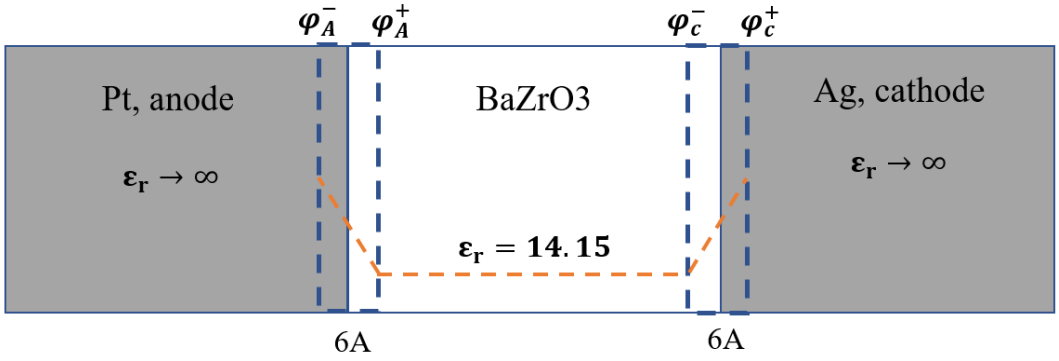

Figure 4.3: Schematic representation of the positions of φ_A^-,φ_A^+,φ_C^-,φ_C^+ and the distribution of ϵ_r. At the interface between the electrode and the electrolyte, ϵ_r is assumed to be linearly varying from 14.15 (at electrolyte side) to 50 (at electrode side).

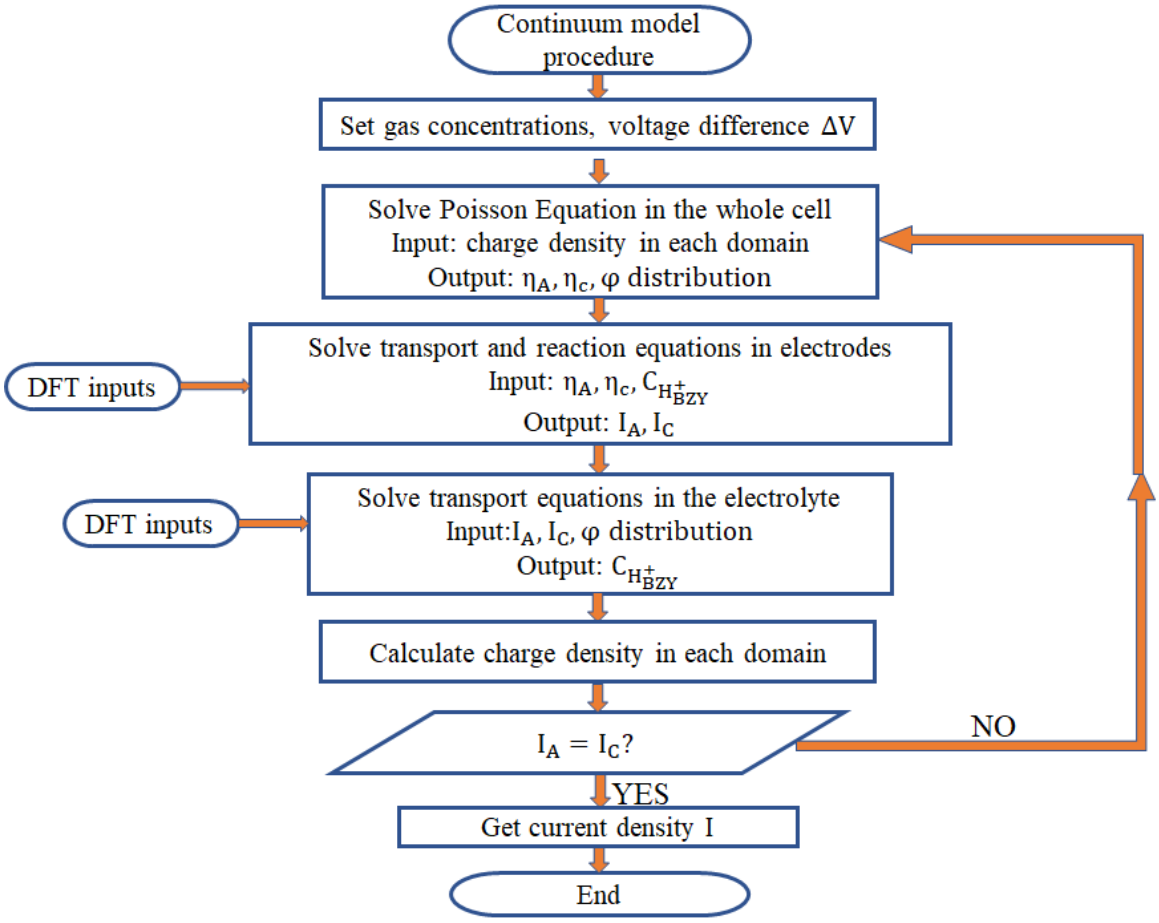

Figure 4.4: Flow chart of the continuum model procedure for proton-conducting SOFC.

Table 4.2: Internal energy barriers and free energy barriers for diffusivities. Here λ is the migration length. The value for $D_{H^+_{BZY}}$ is from experiments, and the value for D_{H_2}, D_{O_2}, D_{H_2O} is from Dusty Gas Model[1].

Parameters	Δ G(T)(eV)	$\lambda \mathring{A}$	Values (s^{-1})
D_{H_2}[1]	/	/	4.3569 $\times 10^{-5}$
D_{O_2}[1]	/	/	1.0892 $\times 10^{-5}$
D_{H_2O}[1]	/	/	1.4523 $\times 10^{-5}$
$D_{H_{2,Pt}}$	0	1.6235	1.5982 $\times 10^{-7}$
$D_{O_{2,Ag}}$	0	1.6985	1.7493 $\times 10^{-7}$
$D_{H_2O_{Ag}}$	0	1.6985	1.7493 $\times 10^{-7}$
$D_{H^+_{Pt}}$	0.0445	1.6235	9.0557 $\times 10^{-8}$
$D_{H^+_{Ag}}$	0.1427	1.6985	2.6283 $\times 10^{-8}$
$D_{O^{2-}_{Ag}}$	0.3448	1.6985	1.796 $\times 10^{-9}$
$D_{OH^-_{Ag}}$	0.2904	1.6985	3.701 $\times 10^{-9}$
$D_{H^+_{BZY}}$[2]	/	/	5.2756 $\times 10^{-10}$

4.3 Simulation Results

4.3.1 DFT Calculation Results

The DFT calculations contain two parts, the free energy barrier calculations for transport steps and the free energy barrier calculations for reaction steps. The detailed energy barrier values are presented in Table 4.2 and Table 4.3.

Figure 4.5 and Table 4.2 show the free energy barriers for the diffusion of different species on metal surfaces. We can see that diffusion on metal surfaces is a fast process with low energy barriers. Therefore, this process is not a rate-limiting process.

Figure 4.6 and Table 4.3 show the reaction configurations and the energy barriers for different reaction steps. From Table 4.3 we can see that, k_4^+, which is the forward reaction rate constant for reaction R4, $H^+_{BZY} \rightarrow H^+_{Ag}$, is much smaller than other rate constants. It means that R4, referring to the direct hopping of H^+ from BZY onto the Ag surface, is not a favorable reaction step. On the contrary, k_5^+ and k_6^+, which are the forward reaction rate constants for reaction R5, $H^+_{BZY} + O^{2-}_{Ag} \rightarrow OH^-_{Ag}$ and R6, $H^+_{BZY} + OH^{2-}_{Ag} \rightarrow H_2O_{Ag}$, are much larger than k_4^+. Since R4, R5 and R6 are all the reaction steps referring to the transport of proton from BZY phase to the Ag surface, it means that steps R5 and R6 are more favorable than R4.

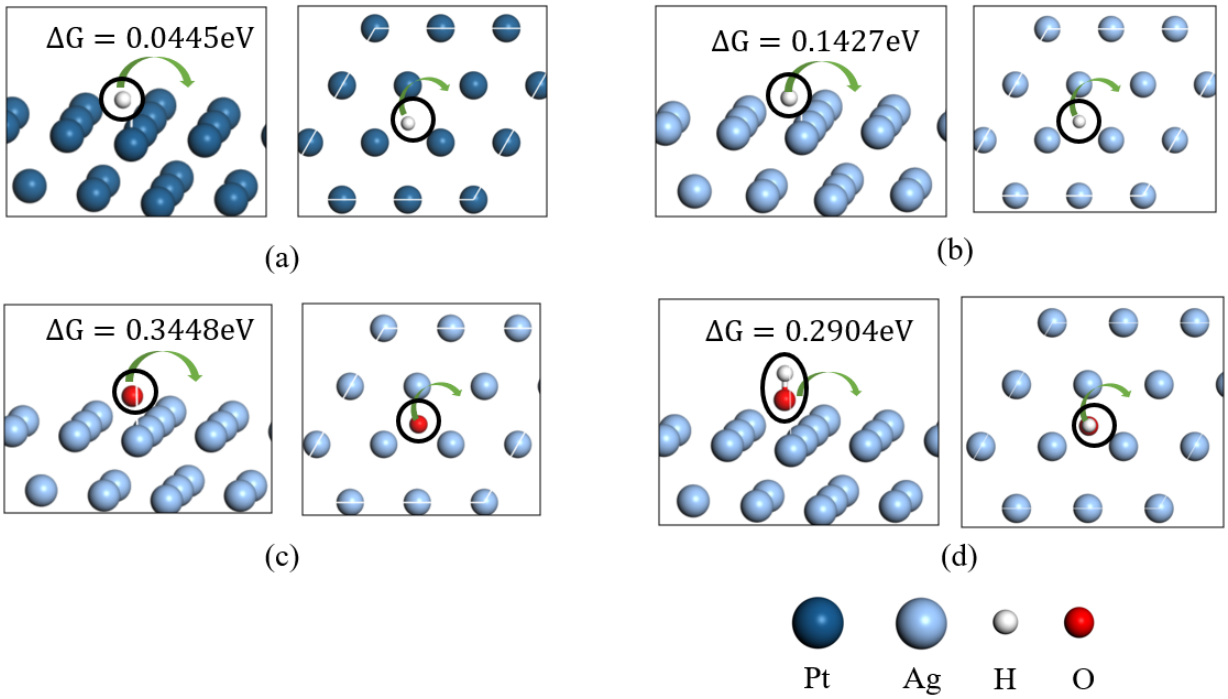

Figure 4.5: Free energy barriers for diffusion on metal surfaces. (a) Free energy barrier for H^+ diffusion on Pt surface. (b) Free energy barrier for H^+ diffusion on Ag surface. (c) Free energy barrier for O^{2-} diffusion on Ag surface. (d) Free energy barrier for OH^- diffusion on Ag surface.

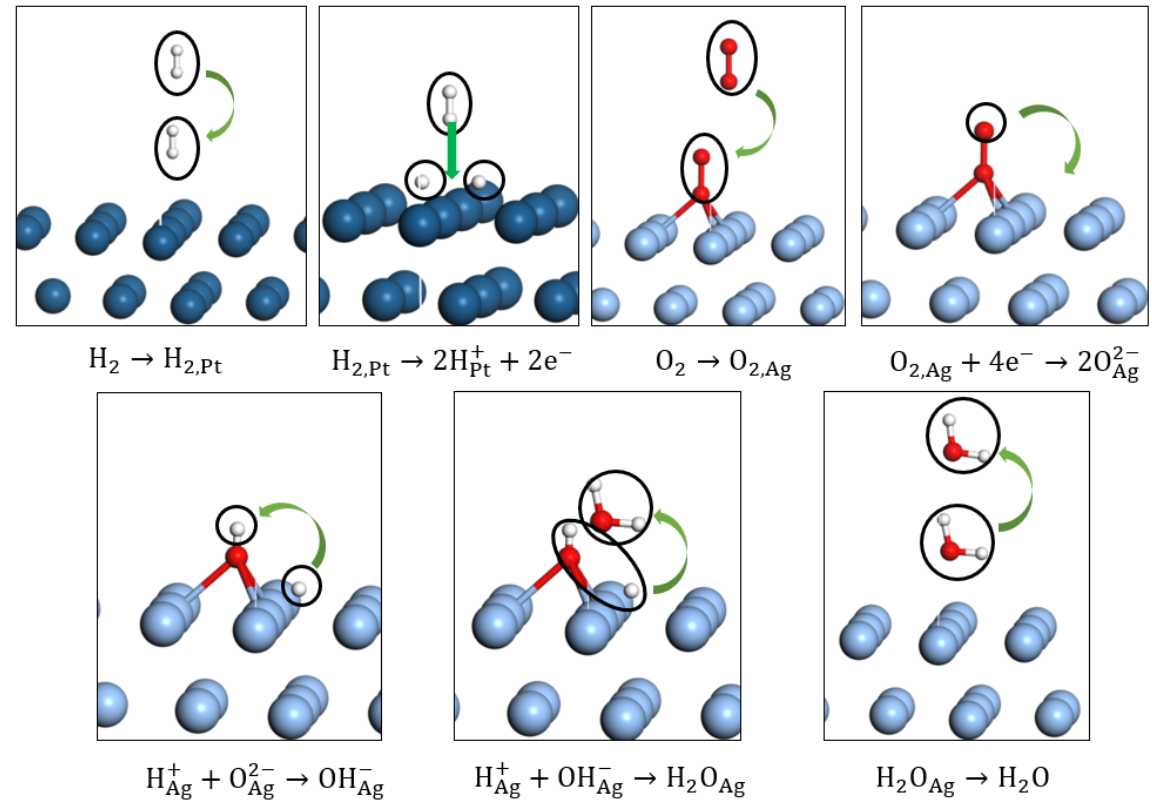

(a)

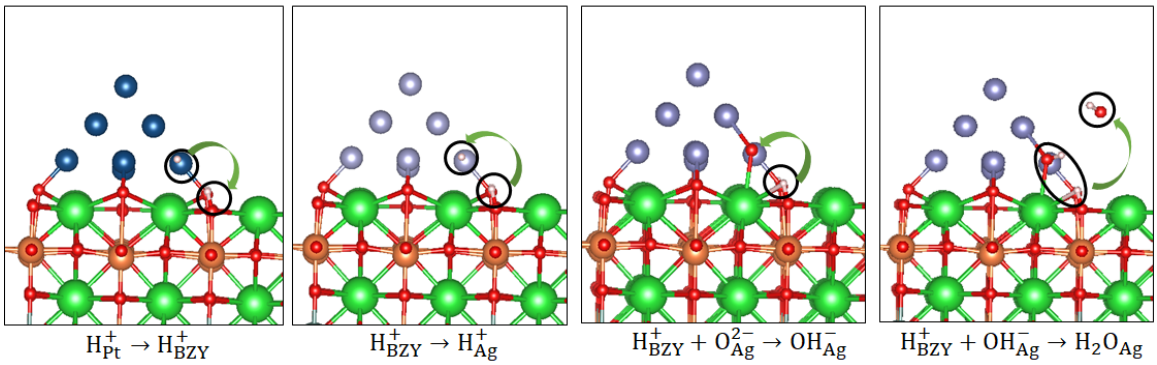

(b)

Figure 4.6: Different reaction configurations used in DFT calculations. (a) Reaction configurations on metal surfaces. (b) Reaction configurations at the meta-BZY-air TPB.

Table 4.3: Internal energy barriers and free energy barriers for each reaction rate constant. $\Delta G(T)$ is the free energy barrier at temperature T=873K.

Parameters	Δ G(T)(eV)	Values (s^{-1})
k_1^+	0.73457	1.05579×10^9
k_1^-	0	1.819×10^{13}
k_2^+	0	1.819×10^{13}
k_2^-	0.49168	3.2637×10^{10}
k_3^+	0	1.819×10^{13}
k_3^-	0.7745	6.209×10^8
k_4^+	1.2725	8.3433×10^5
k_4^-	0	1.819×10^{13}
k_5^+	0.8725	1.6895×10^8
k_5^-	0.9048	1.1010×10^8
k_6^+	0.658	2.9152×10^9
k_6^-	0.291	3.8155×10^{11}
k_7^+	1.1891	2.52527×10^6
k_7^-	0	1.819×10^{13}
k_8^+	0	1.819×10^{13}
k_8^-	0.73497	1.0502×10^9
k_9^+	0	1.819×10^{13}
k_9^-	1.6241	7.8296×10^3
k_{10}^+	0	1.819×10^{13}
k_{10}^-	1.21448	1.8028×10^6
k_{11}^+	0	1.819×10^{13}
k_{11}^-	0.91616	9.47×10^7

4.3.2 Continuum Modeling Results

The current density-voltage loss plot is shown in Figure 4.7, and it is consistent with experimental results. The concentration of different ions and different molecules in the cell with no voltage bias is shown in Figure 4.9 and Figure 4.10. We can see that the concentration variations of these species in the electrodes are very small. On the contrary, we can see proton segregation as well as electron segregation at the electrolyte/electrode interface from Figure 4.8 and Figure 4.9(a). Segregation of protons results in the positive charge at the electrolyte side, while segregation of electrons results in the negative charge at the electrode side. These charges at the electrolyte/electrode interface form the electric double layer, and is the origin of the interfacial overpotential.

Figure 4.11 shows the potential distribution in the cell under different voltage bias. We can see that with the variation of voltage bias, the anode overpotential changes little, while the cathode overpotential varies a lot. It is related to the reaction rate constants of different reaction steps. It can be seen from Table 4.3 that k_3^+, which is the reaction rate constant for protons transporting from the anode surface to the electrolyte, is much larger than k_4^+, k_5^+ and k_6^+, which is the reaction rate constant for protons transporting from the electrolyte to the cathode surface. Therefore, the reactions at the electrolyte/cathode interface are much slower than at the anode/electrolyte interface. This conclusion is consistent with experimental results, showing that the resistance at the electrolyte/cathode interface is larger than that at the anode/electrolyte interface[2].

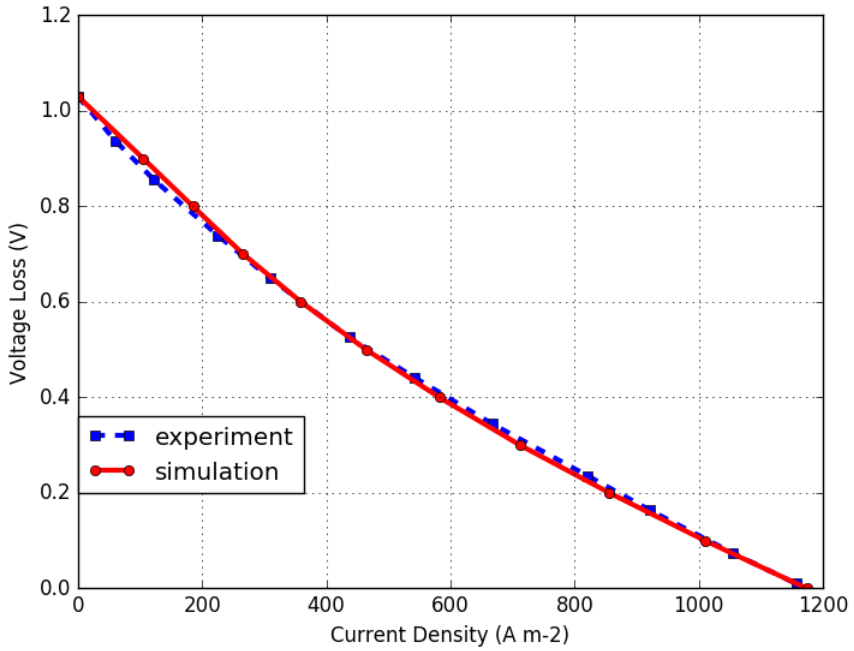

Figure 4.7: Simulation and experimental voltage loss-current density curve under the temperature = 873K.

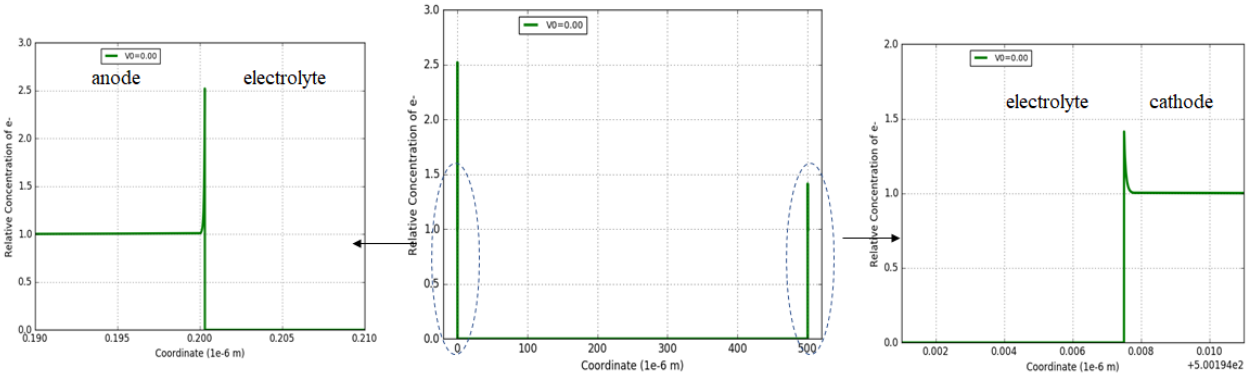

Figure 4.8: Concentration of e^- in the cell with no voltage bias on the boundaries.

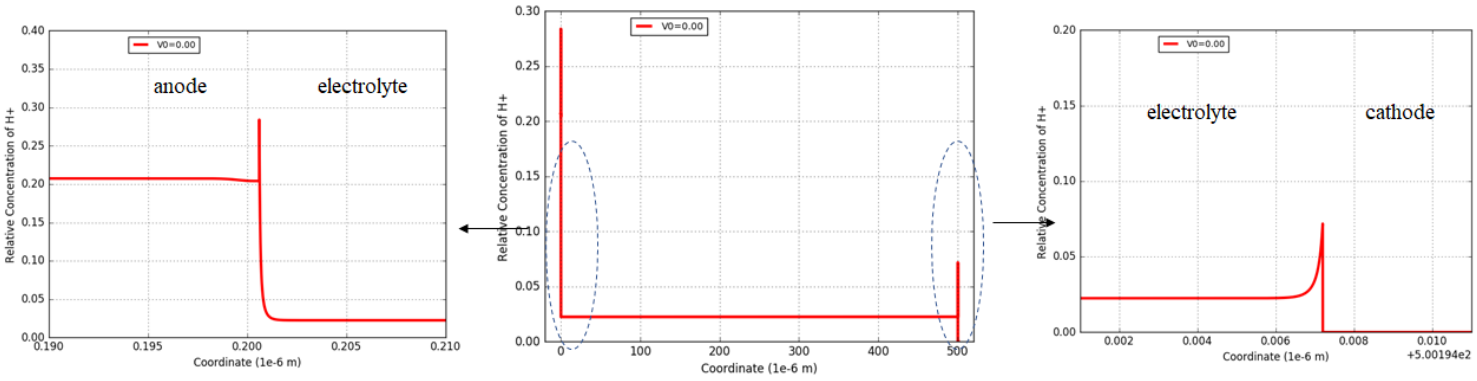

(a)

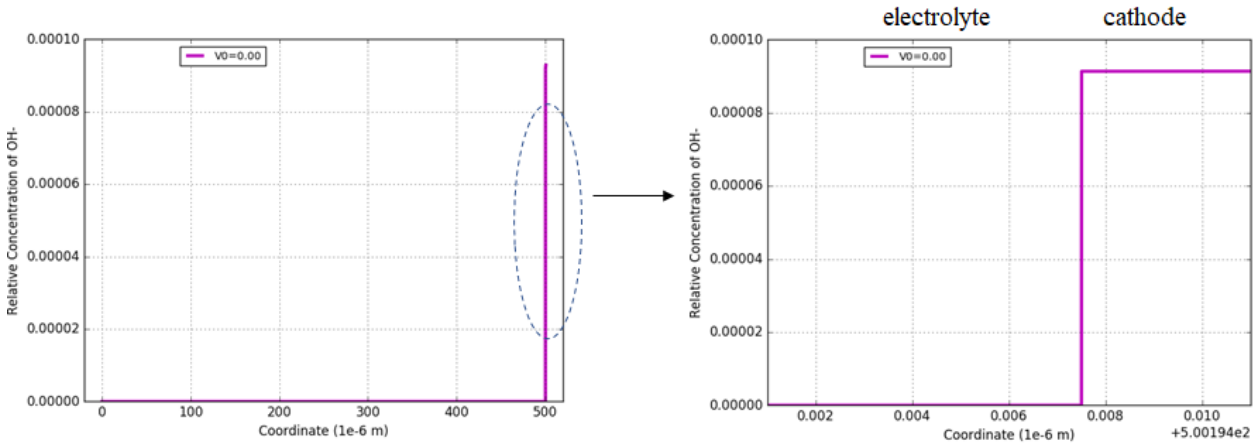

(b)

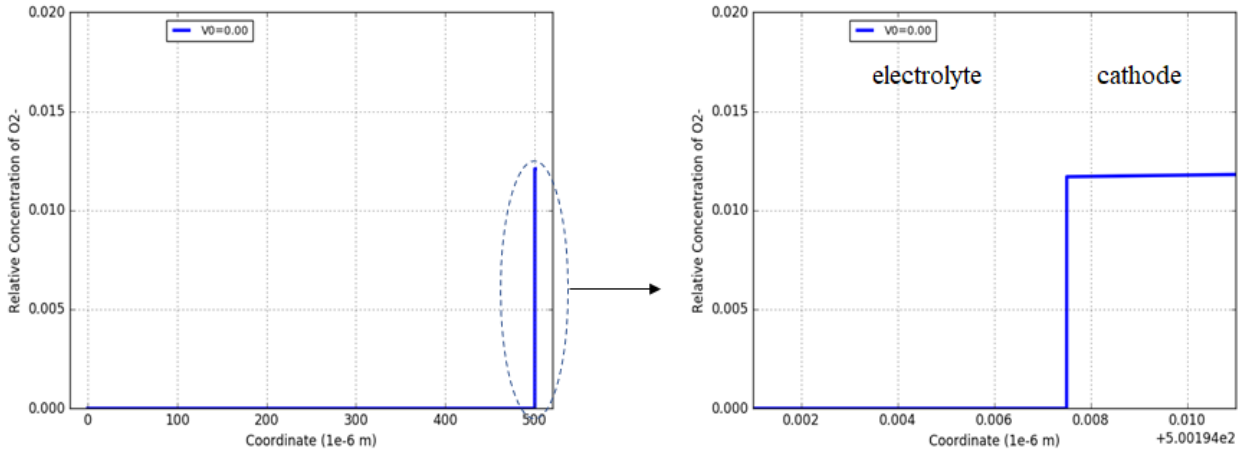

(c)

Figure 4.9: (a) Concentration of H^+ in the cell with no voltage bias on the boundaries. (b) Concentration of OH^- in the cell with no voltage bias on the boundaries. (c) Concentration of O^{2-} in the cell with no voltage bias on the boundaries.

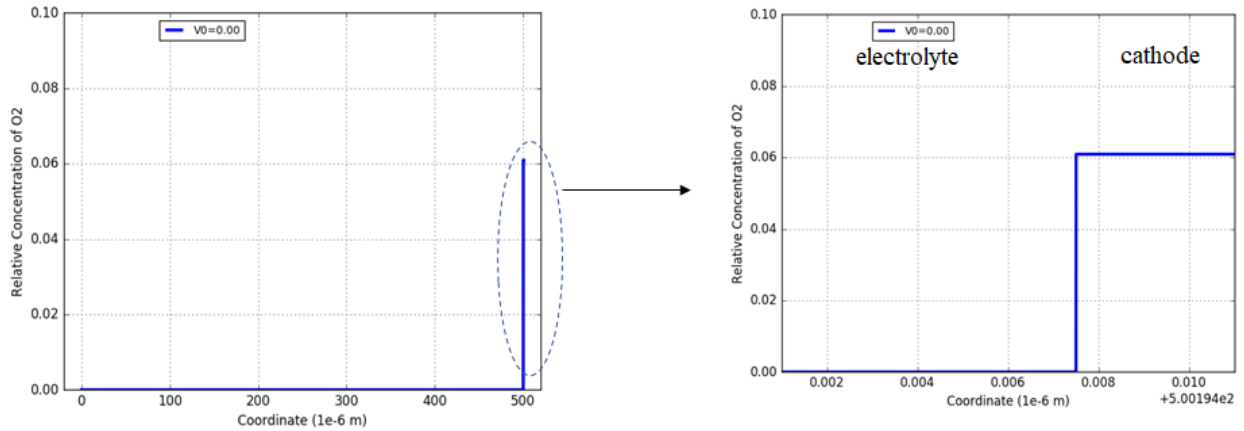

(a)

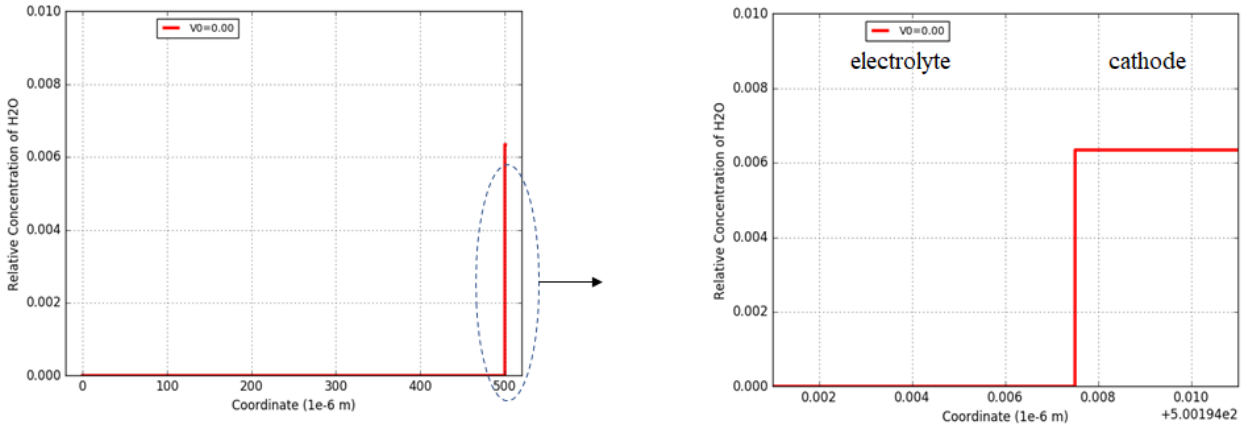

(b)

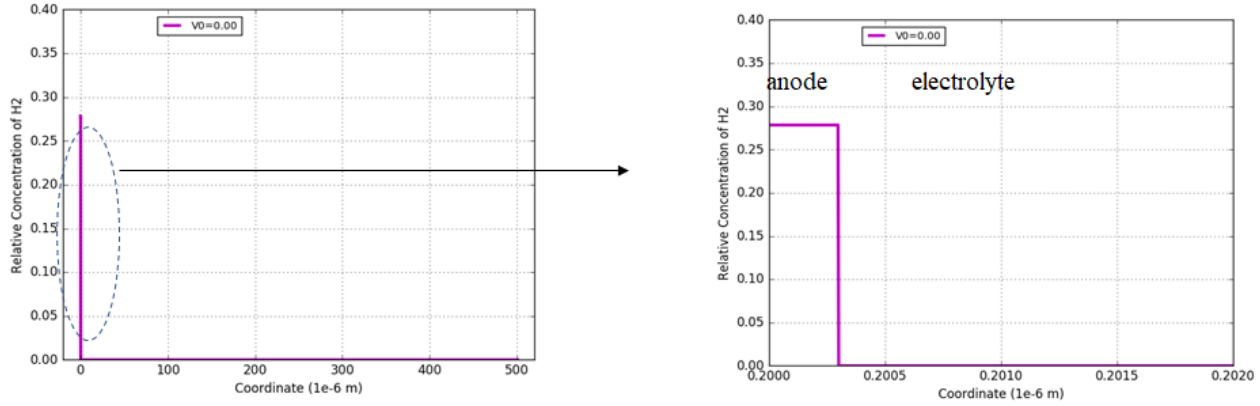

(c)

Figure 4.10: (a) Concentration of O_2 in the cell with no voltage bias on the boundaries. (b) Concentration of H_2O in the cell with no voltage bias on the boundaries. (c) Concentration of H_2 in the cell with no voltage bias on the boundaries.

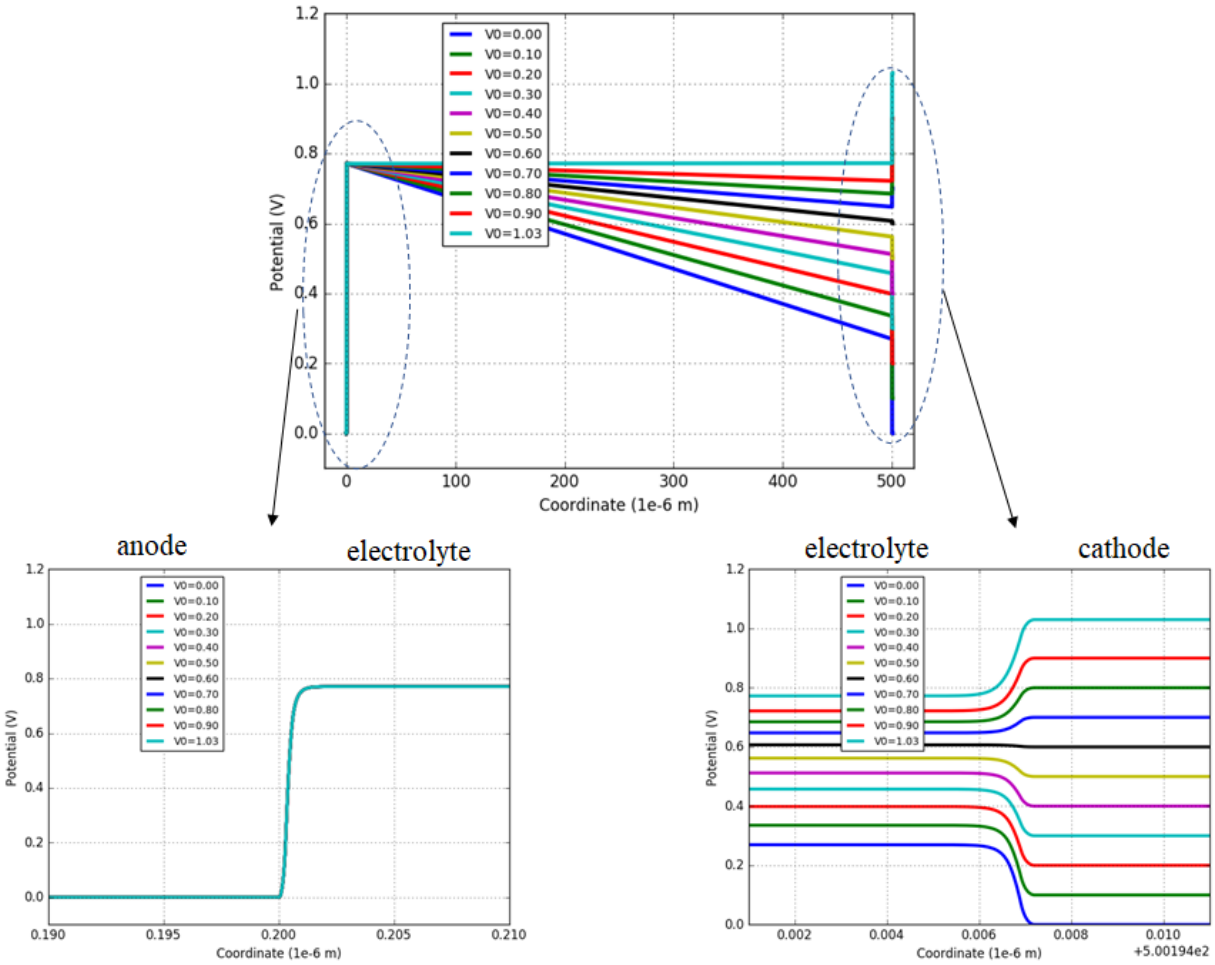

Figure 4.11: Potential distribution in the cell under different voltage bias.

CHAPTER 5

CONCLUSION

In summary, we developed a multiscale model combining DFT-based calculations, transition state theory and continuum modeling to elucidate the essential reaction steps and predict the performance of the oxide ion as well as proton-conducting solid oxide cells.

As to the oxide ion-conducting SOCs, we developed a model for the oxygen reduction and oxidation reactions in LSCF based solid oxide fuel and electrolysis cells, respectively. DFT+U calculations were used to obtain the energy barriers for different reaction steps. The influence of concentration on free energy barrier for specific steps was considered based on the published experimental results. Transition state theory was used to predict the reaction rate constants for each step based on the free energy barrier. Continuum modeling utilized the reaction rate constants, diffusivities and LSCF microstructure parameters and predicted the overpotential-current density relations. The proposed model results are consistent with overpotential-current density data from experiments. We found that oxygen exchange at the TPB can be neglected in our model. Chemical reaction of surface oxygen molecules split under SOFC mode / surface oxide ions combination under SOEC mode is the essential reaction step, and oxide ion diffusion in bulk LSCF is the essential diffusion step. We also highlight that SrO terminated LSCF surface is not an efficient surface structure for oxygen oxidation and reduction reactions.

As to the proton-conducting SOCs, we developed a model for the Pt/BZY/Ag based solid oxide fuel cell. DFT calculations were used to obtain the energy barriers for different reaction steps. Transition state theory was used to predict the reaction rate constants for each step based on the free energy barrier. Continuum modeling utilized the reaction rate constants, diffusivities and microstructure parameters and predicted the voltage loss-current density relations. The proposed model results are consistent with the experi-

mental data. We also found that the cathode reactions are more rate-limiting than the anode reactions.

APPENDIX A

DERIVATIONS OF SPECIFIC EQUATIONS

In this chapter, the derivation of the electric potential gradient equation, which is equation (3.9), and the derivation of the concentration dependent free energy expressions, which are equations (3.19,3.20) are presented.

A.1 Derivation of the Electric Potential Gradient Equation

The current density distribution is presented in Figure A.1. At the top boundary, the ionic current density is 0, and the overall current density is from the electronic conduction. At the bottom boundary, the overall current density is from the ionic conduction. According to the current density conservation equation, we have that

$$I(O^{2-}) + I(e^{-}) = I(O^{2-})(bottom) \tag{A.1}$$

where

$$I(O^{2-}) = 2F_a D_{O^{2-}}(\frac{d}{dz}C_{O^{2-}} - \frac{2F_a C_{O^{2-}}}{RT}\frac{d}{dz}\varphi) \tag{A.2}$$

$$I(e^{-}) = -\sigma\frac{d}{dz}\varphi \tag{A.3}$$

$$I(O^{2-})(bottom) = 2F_a D_{O^{2-}}\frac{d}{dz}C_{O^{2-}}(bottom) \tag{A.4}$$

After putting equations (A.2 - A.4) into (A.1), we can get

$$\frac{d}{dz}\varphi = \frac{2F_a D_{O^{2-}}(\frac{d}{dz}C_{O^{2-}} - \frac{d}{dz}C_{O^{2-}}(bottom))}{\sigma + \frac{4{F_a}^2 C_{O^{2-}} D_{O^{2-}}}{RT}} \tag{A.5}$$

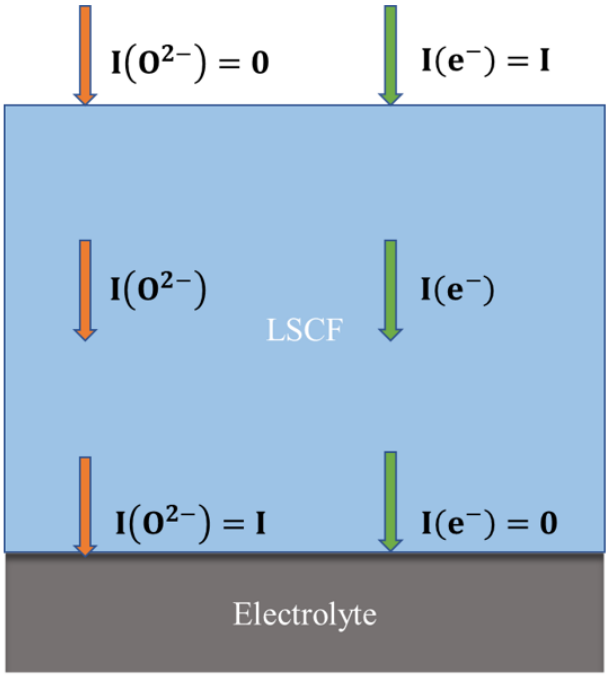

(a)

Figure A.1: Schematic representation of current density distribution in LSCF. $I(O^{2-})$ is the current density from oxide ion conduction, and $I(e^{-})$ is the current density from electronic conduction.

A.2 Derivation of the Concentration Dependent Free Energy Expressions

The equation for oxygen vacancy formation in bulk LSCF is as follows:

$$\mathrm{O^{2-}} \rightarrow \mathrm{V_O} + 0.5\mathrm{O_2} + 2\mathrm{e^-}$$

The relation between the concentrations of O^{2-}, V_O and O_2 and the vacancy formation energy are as follows:

$$C_{O_2}^{0.5}\frac{C_{V_O}}{C_{O^{2-}}^{max} - C_{V_O}} = \exp(-\frac{\Delta G_{f,vac}}{k_B T}) = \exp(-\frac{\Delta G_{f,vac}^{perf} + a\frac{C_{V_O}}{C_{O^{2-}}^{max}}}{k_B T}) \tag{A.6}$$

$$\ln(C_{O_2}) = -2\frac{\Delta G_{f,vac}^{perf} + a\frac{C_{V_O}}{C_{O^{2-}}^{max}}}{k_B T} - 2\ln(\frac{C_{V_O}}{C_{O^{2-}}^{max} - C_{V_O}}) \tag{A.7}$$

According to reference [54], the relation between oxide ion diffusivity and C_{O_2} are as follows:

$$D_{O^{2-}} = \frac{\lambda^2}{6}\frac{k_B T}{h}\exp(-\frac{\Delta G_{D_{O^{2-}}}(T)}{k_B T})\exp(-\frac{\Delta G_{D_{O^{2-}}}(C_{V_O})}{k_B T}) \propto C_{O_2}^{\gamma_{bulk}} \tag{A.8}$$

Therefore

$$\Delta G_{D_{O^{2-}}}(C_{V_O}) = -\gamma_{bulk} k_B T \ln(C_{o_2}) + const \tag{A.9}$$

After putting equation (A.7) into equation (A.9), we have

$$\Delta G_{D_{O^{2-}}}(C_{V_O}) = 2\gamma_{bulk}(\Delta G_{f,vac}^{perf} + a\frac{C_{V_O}}{C_{O^{2-}}^{max}}) + 2\gamma_{bulk} k_B T \ln(\frac{C_{V_O}}{C_{O^{2-}}^{max} - C_{V_O}}) + const \tag{A.10}$$

For $2\gamma_{bulk}\Delta G_{f,vac}^{perf}$ term is a constant (not a function of concentration), and $\gamma_{bulk} k_B T \ln(\frac{C_{V_O}}{C_{O^{2-}}^{max} - C_{V_O}}) << \gamma_{bulk} a\frac{C_{V_O}}{C_{O^{2-}}^{max}}$, we have

$$\Delta G_{D_{O^{2-}}}(C_{V_O}) = 2\gamma_{bulk} a\frac{C_{V_O}}{C_{O^{2-}}^{max}} + const \tag{A.11}$$

Considering that in equilibrium, $\Delta G_{D_{O^{2-}}}(C_{V_O}) = 0$, we have

$$\Delta G_{D_{O^{2-}}}(C_{V_O}) = 2\gamma_{bulk} a \frac{(C_{V_O} - C_{V_O}^{equi})}{C_{O^{2-}}^{max}} = 2\gamma_{bulk} a \frac{\Delta C_{V_O}}{C_{O^{2-}}^{max}} \tag{A.12}$$

Where $C_{V_O}^{equi}$ is the vacancy concentration in bulk LSCF in equilibrium, which is about 600 mol/m^3. The relation between $k_{3,suf}^{+}$,$k_{3,suf}^{-}$ and C_{O_2} are as follows:

$$k_{3,suf}^{+}, k_{3,suf}^{-} \propto C_{O_2}^{\gamma_{surf}} \tag{A.13}$$

After derivations similar to equations (A.8 - A.10), we have

$$\Delta G_{k_{3,suf}^{+}}(C_{V_O}) = \Delta G_{k_{3,suf}^{-}}(C_{V_O}) = 2\gamma_{suf} a \frac{C_{V_O}}{C_{O^{2-}}^{max}} + const \tag{A.14}$$

Considering that when $C_{V_O} = C_{V_O}^{DFT}$, $k_{3,suf}^{+} = \frac{k_B T}{h} \exp(-\frac{\Delta G_{k_{3,suf}^{+}}^{(T)}}{k_B T})$, $k_{3,suf}^{-} = \frac{k_B T}{h} \exp(-\frac{\Delta G_{k_{3,suf}^{-}}^{(T)}}{k_B T}))$, we have

$$\Delta G_{k_{3,suf}^{+}}(C_{V_O}) = \Delta G_{k_{3,suf}^{-}}(C_{V_O}) = 2\gamma_{suf} a \frac{(C_{V_O} - C_{V_O}^{DFT})}{C_{O^{2-}}^{max}} = 2\gamma_{suf} a \frac{\Delta C_{V_O}}{C_{O^{2-}}^{max}} \tag{A.15}$$

Where $C_{V_O}^{DFT}$ is the vacancy concentration in bulk LSCF used in the DFT calculations, which is about 1154 mol/m^3.

APPENDIX B

DEFINITIONS FOR INTERFACE AND SUBSURFACE LAYERS

In this chapter, we present the definitions for interface and subsurface layers, which are used in chapter 3. The positions for different oxide ions and vacancies are presented in Figure B.1. Because oxide ions can only migrate from one layer to its neighboring layer, the reactions R4 and R5 in chapter 3 consist of multiple migration steps across different layers. As to the LSCF surface structure, the 4th atom layer is regarded as the bulk layer. As to the interface structure, the 1st atom layer is regarded as the LSCF bulk layer, the 7th atom layer is regarded as the electrolyte bulk layer, and all the layers in between are regarded as the interfacial layers.

The reaction rate expressions for the migrations of oxide ions from surface to the bulk are as follows:

$$r_{R4}^{suf\rightarrow sub_1} = A_{suf}[k_{4_1,suf}^{+} C_{O_{suf}^{-}} \frac{C_{V_O^{sub_1}}}{C_{O_{suf}^{2-}}^{max}} - k_{4_1,suf}^{-} C_{O_{sub_1}^{2-}} \frac{C_{V_O^{suf}}}{C_{O_{suf}^{2-}}^{max}}] \tag{B.1}$$

$$r_{R4}^{sub_1\rightarrow sub_2} = A_{suf}[k_{4_2,suf}^{+} C_{O_{sub_1}^{2-}} \frac{C_{V_O^{sub_2}}}{C_{O_{suf}^{2-}}^{max}} - k_{4_2,suf}^{-} C_{O_{sub_2}^{2-}} \frac{C_{V_O^{sub_1}}}{C_{O_{suf}^{2-}}^{max}}] \tag{B.2}$$

$$r_{R4}^{sub_2\rightarrow bulk} = A_{suf}[k_{4_3,suf}^{+} C_{O_{sub_2}^{2-}} \frac{C_{V_O}}{C_{O^{2-}}^{max}} - k_{4_3,suf}^{-} C_{O^{2-}} \frac{C_{V_O^{sub_2}}}{C_{O^{2-}}^{max}}] \tag{B.3}$$

where $suf \rightarrow sub_1$ denotes the migration of oxide ions from the surface to the first subsurface layer, $sub_1 \rightarrow sub_2$ denotes the migration of oxide ions from the first subsurface layer to the second subsurface layer, and $sub_2 \rightarrow bulk$ denotes the migration of oxide ions from the second subsurface layer to the bulk. When the reactions reach the steady state, we have

$$r_{R4}^{suf\rightarrow sub_1} = r_{R4}^{sub_1\rightarrow sub_2} = r_{R4}^{sub_2\rightarrow bulk} = r_{R4}^{suf} \tag{B.4}$$

The values for $C_{V_O^{sub_1}}$ and $C_{O^{2-}_{sub_1}}$ can be obtained after solving equation (B.4). After that we can put these two values in the equation (3.13) to get r_{R4}^{suf}.

The reaction rate expressions for the migrations of oxide ions across the LSCF/GDC interface are as follows:

$$r_{R5}^{bulk\to int_1} = A_{int}[k_{1,int}^{+} C_{V_O^{int_1}} \frac{C_{O^{2-}}}{C_{O^{2-}}^{max}} - k_{1,int}^{-} C_{O^{2-}_{int_1}} \frac{C_{V_O}}{C_{O^{2-}}^{max}}] \tag{B.5}$$

$$r_{R5}^{int_1\to int_2} = A_{int}[k_{2,int}^{+} C_{V_O^{int_2}} \frac{C_{O^{2-}_{int_1}}}{C_{O^{2-}}^{max}} - k_{2,int}^{-} C_{O^{2-}_{int_2}} \frac{C_{V_O}^{int_1}}{C_{O^{2-}}^{max}}] \tag{B.6}$$

$$r_{R5}^{int_2\to int_3} = A_{int}[k_{3,int}^{+} C_{V_O^{int_3}} \frac{C_{O^{2-}_{int_2}}}{C_{O^{2-}}^{max}} - k_{3,int}^{-} C_{O^{2-}_{int_3}} \frac{C_{V_O}^{int_2}}{C_{O^{2-}}^{max}}] \tag{B.7}$$

$$r_{R5}^{int_3\to int_4} = A_{int}[k_{4,int}^{+} \exp(-\frac{2F_a\eta}{RT}) C_{V_O^{int_4}} \frac{C_{O^{2-}_{int_3}}}{C_{O^{2-}}^{max}} - k_{4,int}^{-} C_{O^{2-}_{int_4}} \frac{C_{V_O}^{int_3}}{C_{O^{2-}}^{max}}] \tag{B.8}$$

$$r_{R5}^{int_4\to int_5} = A_{int}[k_{5,int}^{+} C_{V_O^{int_5}} \frac{C_{O^{2-}_{int_4}}}{C_{O^{2-}}^{max}} - k_{5,int}^{-} C_{O^{2-}_{int_5}} \frac{C_{V_O}^{int_4}}{C_{O^{2-}}^{max}}] \tag{B.9}$$

$$r_{R5}^{int_5\to ele} = A_{int}[k_{6,int}^{+} C_{V_O^{ele}} \frac{C_{O^{2-}_{int_5}}}{C_{O^{2-}}^{max}} - k_{6,int}^{-} C_{O^{2-}_{ele}} \frac{C_{V_O}^{int_5}}{C_{O^{2-}}^{max}}] \tag{B.10}$$

where $bulk \to int_1$ denotes the migration of oxide ions from the bulk LSCF to the first interfacial layer, $int_i \to int_j$ denotes the migration of oxide ions from the ith interfacial layer to the jth interfacial layer, and $int_5 \to ele$ denotes the migration of oxide ions from the fifth interfacial layer to the bulk electrolyte. The overpotential η is added on the reaction rate $r_{R5}^{int_3\to int_4}$, for the third and fourth interfacial layers are the interacting layers between LSCF and GDC, and the interface electric double layer induced overpotential acts between them. When the reactions reach the steady state, we have

$$r_{R5}^{bulk\to int_1} = r_{R5}^{int_1\to int_2} = r_{R5}^{int_2\to int_3} = r_{R5}^{int_3\to int_4} = r_{R5}^{int_4\to int_5} = r_{R5}^{int_5\to ele} = r_{R5}^{int_5} \tag{B.11}$$

The values for $C_{V_O^{int_1}}$ and $C_{O^{2-}_{int_1}}$ can be obtained after solving equation (B.11). After that we can put these two values in the equation (3.14) to get

r_{R5}^{int}.

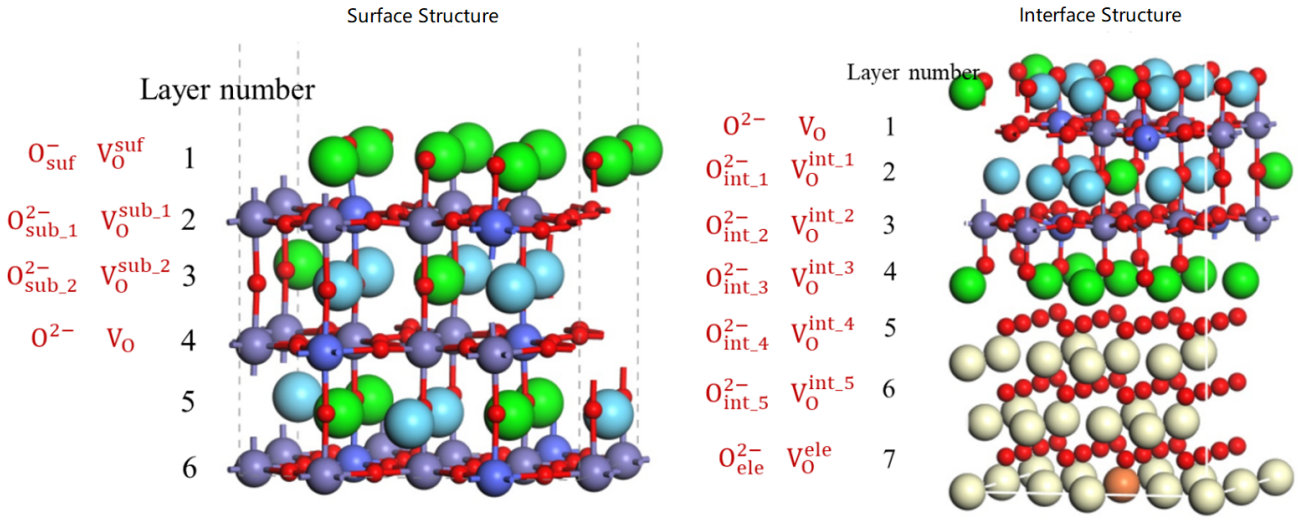

(a)

Figure B.1: Schematic representation of the positions of oxide ions and vacancies in different subsurface and interfacial layers.

APPENDIX C

THE OPTIMIZED STRUCTURES AND THE DETAILS OF EACH REACTION STEP

In this chapter, we present the details of DFT+U calculation results for reaction R1-R5 in chapter 3. The detailed optimized structures and the energy barriers for each reaction steps are presented in Figure C.1 - C.5, respentively.

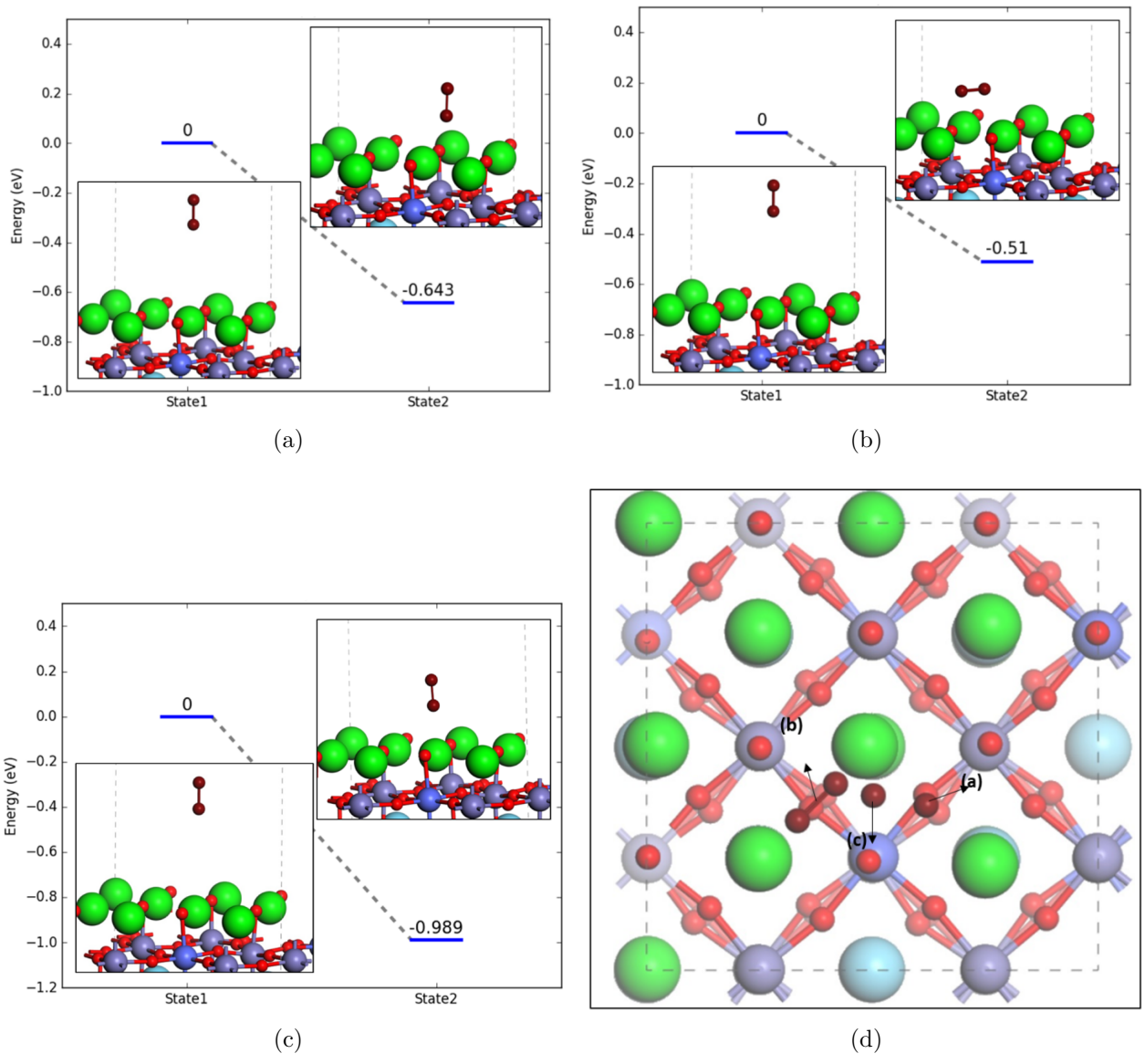

Figure C.1: Energy profile for reaction R1 in Chapter 3. (a-c) The energy profiles with 3 different final optimized structures. The energy difference used in Table 3.2 is the average value of these three results. (d) Top view of the adsorbed oxygen molecule on LSCF surface.

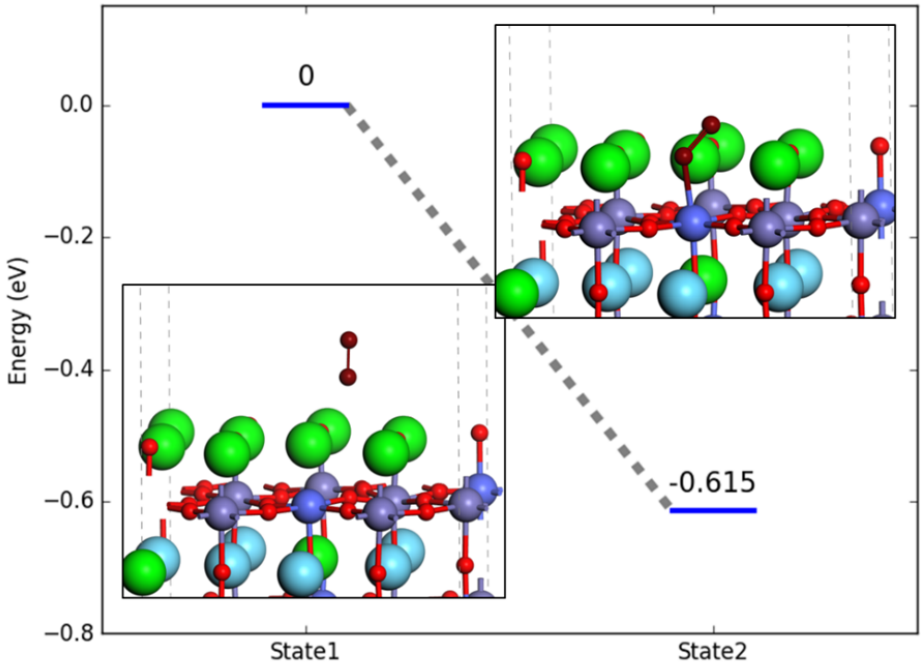

(a)

Figure C.2: Energy profile for reaction R2 in Chapter 3.

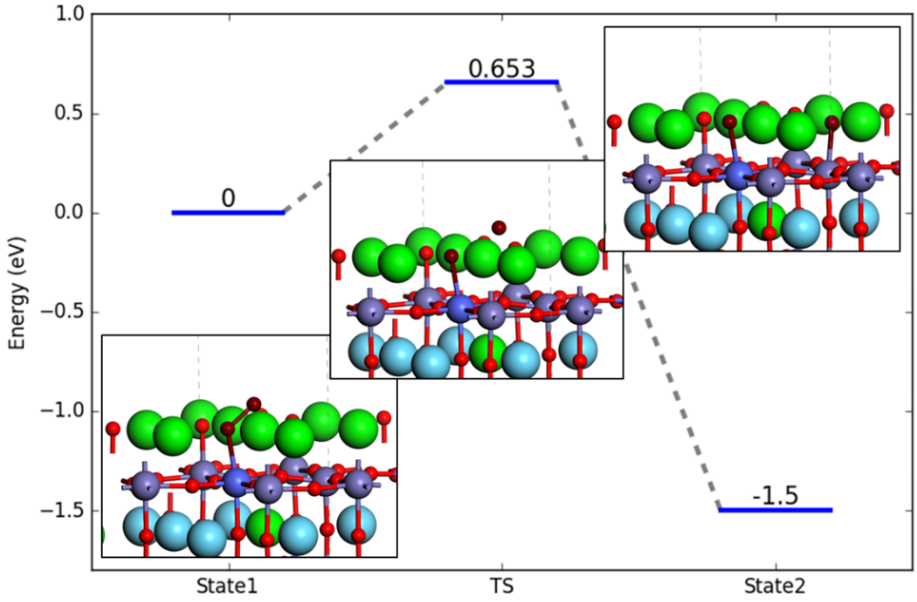

(a)

Figure C.3: Energy profile for reaction R3 in Chapter 3.

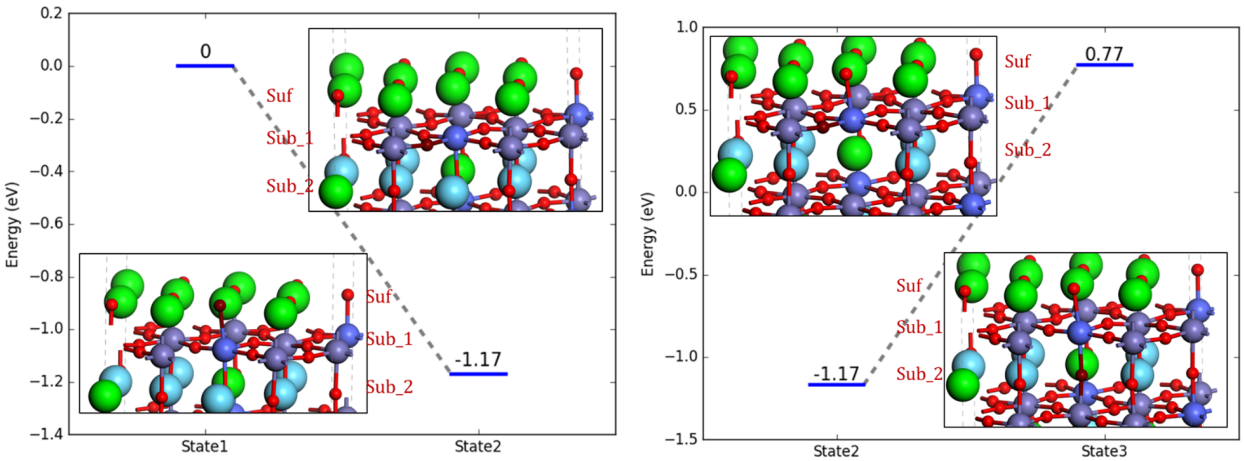

(a)

(b)

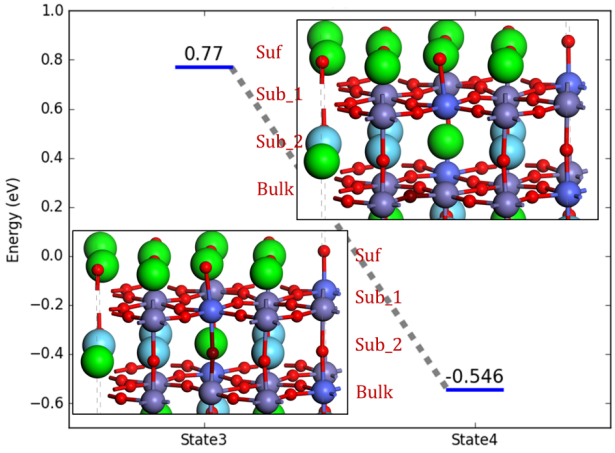

(c)

Figure C.4: Energy profile for reaction R4 in Chapter 3. (a) Migration of an oxide ion from surface to the first subsurface layer. (b) Migration of an oxide ion from the first subsurface layer to the second subsurface layer. (c) Migration of an oxide ion from the second subsurface layer to the third subsurface layer.

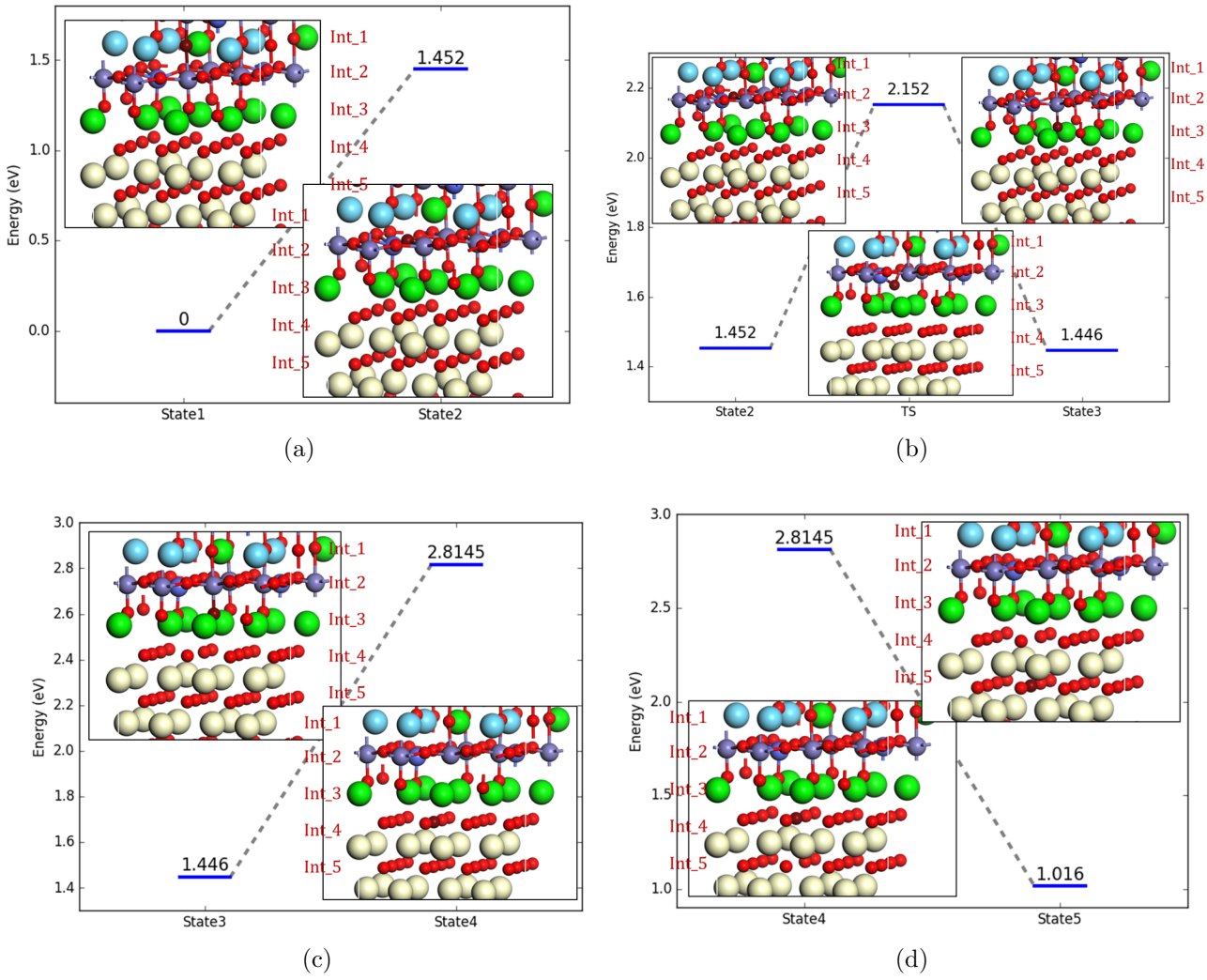

Figure C.5: Energy profile for reaction R5 in Chapter 3. (a) Migration of an oxide ion from the first interfacial layer to the second interfacial layer. (b) Migration of an oxide ion from the second interfacial layer to the third interfacial layer. (c) Migration of an oxide ion from the third interfacial layer to the fourth interfacial layer. (d) Migration of an oxide ion from the fourth interfacial layer to the fifth interfacial layer.

REFERENCES

[1] J. Laurencin, M. Hubert, K. Couturier, T. Le Bihan, P. Cloetens, F. Lefebvre-Joud, and E. Siebert, "Reactive mechanisms of lscf single-phase and lscf-cgo composite electrodes operated in anodic and cathodic polarisations," *Electrochimica Acta*, vol. 174, pp. 1299–1316, 2015.

[2] F. Iguchi, M. Nagai, N. Sata, and H. Yugami, "Fabrication and generation of intermediate temperature operating sofc based on y-doped bazro3 proton conducting oxides," *ECS Transactions*, vol. 25, no. 2, pp. 1759–1766, 2009.

[3] L. Bi, S. Boulfrad, and E. Traversa, "Steam electrolysis by solid oxide electrolysis cells (soecs) with proton-conducting oxides," *Chemical Society Reviews*, vol. 43, no. 24, pp. 8255–8270, 2014.

[4] J. T. Irvine, D. Neagu, M. C. Verbraeken, C. Chatzichristodoulou, C. Graves, and M. B. Mogensen, "Evolution of the electrochemical interface in high-temperature fuel cells and electrolysers," *Nature Energy*, vol. 1, p. 15014, 2016.

[5] S. B. Adler, "Factors governing oxygen reduction in solid oxide fuel cell cathodes," *Chemical reviews*, vol. 104, no. 10, pp. 4791–4844, 2004.

[6] Z. Cheng, J.-H. Wang, Y. Choi, L. Yang, M. Lin, and M. Liu, "From ni-ysz to sulfur-tolerant anode materials for sofcs: electrochemical behavior, in situ characterization, modeling, and future perspectives," *Energy & Environmental Science*, vol. 4, no. 11, pp. 4380–4409, 2011.

[7] Z. Gao, L. V. Mogni, E. C. Miller, J. G. Railsback, and S. A. Barnett, "A perspective on low-temperature solid oxide fuel cells," *Energy & Environmental Science*, vol. 9, no. 5, pp. 1602–1644, 2016.

[8] Y. Zheng, J. Wang, B. Yu, W. Zhang, J. Chen, J. Qiao, and J. Zhang, "A review of high temperature co-electrolysis of h2o and co2 to produce sustainable fuels using solid oxide electrolysis cells (soecs): advanced materials and technology," *Chemical Society Reviews*, vol. 46, no. 5, pp. 1427–1463, 2017.

[9] M. Laguna-Bercero, "Recent advances in high temperature electrolysis using solid oxide fuel cells: A review," *Journal of Power Sources*, vol. 203, pp. 4–16, 2012.

[10] A. Hauch, S. D. Ebbesen, S. H. Jensen, and M. Mogensen, "Highly efficient high temperature electrolysis," *Journal of Materials Chemistry*, vol. 18, no. 20, pp. 2331–2340, 2008.

[11] T. Ishihara, N. Jirathiwathanakul, and H. Zhong, "Intermediate temperature solid oxide electrolysis cell using lagao3 based perovskite electrolyte," *Energy & Environmental Science*, vol. 3, no. 5, pp. 665–672, 2010.

[12] Y. Teraoka, T. Nobunaga, K. Okamoto, N. Miura, and N. Yamazoe, "Influence of constituent metal cations in substituted lacoo3 on mixed conductivity and oxygen permeability," *Solid State Ionics*, vol. 48, no. 3-4, pp. 207–212, 1991.

[13] B. C. Steele and A. Heinzel, "Materials for fuel-cell technologies," *Nature*, vol. 414, no. 6861, pp. 345–352, 2001.

[14] A. J. Jacobson, "Materials for solid oxide fuel cells," *Chemistry of Materials*, vol. 22, no. 3, pp. 660–674, 2009.

[15] E. Fabbri, D. Pergolesi, and E. Traversa, "Materials challenges toward proton-conducting oxide fuel cells: a critical review," *Chemical Society Reviews*, vol. 39, no. 11, pp. 4355–4369, 2010.

[16] C. Zuo, S. Zha, M. Liu, M. Hatano, and M. Uchiyama, "Ba(zr0.1ce0.7y0.2)o3-δ as an electrolyte for low-temperature solid-oxide fuel cells," *Advanced Materials*, vol. 18, no. 24, pp. 3318–3320, 2006.

[17] L. Bi, E. Fabbri, Z. Sun, and E. Traversa, "Bazr0.8y0.2o3-δ-nio composite anodic powders for proton-conducting sofcs prepared by a combustion method," *Journal of The Electrochemical Society*, vol. 158, no. 7, pp. B797–B803, 2011.

[18] H. J. Hwang, J.-W. Moon, S. Lee, and E. A. Lee, "Electrochemical performance of lscf-based composite cathodes for intermediate temperature sofcs," *Journal of Power Sources*, vol. 145, no. 2, pp. 243–248, 2005.

[19] D. Rembelski, J.-P. Viricelle, L. Combemale, and M. Rieu, "Characterization and comparison of different cathode materials for sc-sofc: Lsm, bscf, ssc, and lscf," *Fuel Cells*, vol. 12, no. 2, pp. 256–264, 2012.

[20] W. Yang, Z. Wang, Z. Wang, Z. Yang, C. Xia, R. Peng, X. Wu, and Y. Lu, "Enhanced catalytic activity toward o2 reduction on pt-modified la1-xsrxco1-yfeyo3-δ cathode: A combination study of first-principles calculation and experiment," *ACS applied materials & interfaces*, vol. 6, no. 23, pp. 21 051–21 059, 2014.

[21] B. Ingram, J. Eastman, K.-C. Chang, S. Kim, T. Fister, E. Perret, H. You, P. Baldo, and P. Fuoss, "In situ x-ray studies of oxygen surface exchange behavior in thin film la0.6sr0.4co0.2fe0.8o3-δ," *Applied Physics Letters*, vol. 101, no. 5, p. 051603, 2012.

[22] F. Baumann, J. Fleig, G. Cristiani, B. Stuhlhofer, H.-U. Habermeier, and J. Maier, "Quantitative comparison of mixed conducting sofc cathode materials by means of thin film model electrodes," *Journal of The Electrochemical Society*, vol. 154, no. 9, pp. B931–B941, 2007.

[23] N. Grunbaum, L. Dessemond, J. Fouletier, F. Prado, L. Mogni, and A. Caneiro, "Rate limiting steps of the porous la0.6sr0.4co0.8fe0.2o3-δ electrode material," *Solid State Ionics*, vol. 180, no. 28, pp. 1448–1452, 2009.

[24] T. Akbay, A. Staykov, J. Druce, H. Téllez, T. Ishihara, and J. A. Kilner, "The interaction of molecular oxygen on lao terminated surfaces of la2nio4," *Journal of Materials Chemistry A*, vol. 4, no. 34, pp. 13 113–13 124, 2016.

[25] A. Staykov, H. Tellez, T. Akbay, J. Druce, T. Ishihara, and J. Kilner, "Oxygen activation and dissociation on transition metal free perovskite surfaces," *Chemistry of Materials*, vol. 27, no. 24, pp. 8273–8281, 2015.

[26] A. Chroneos, B. Yildiz, A. Tarancón, D. Parfitt, and J. A. Kilner, "Oxygen diffusion in solid oxide fuel cell cathode and electrolyte materials: mechanistic insights from atomistic simulations," *Energy & Environmental Science*, vol. 4, no. 8, pp. 2774–2789, 2011.

[27] W. Paulus, H. Schober, S. Eibl, M. Johnson, T. Berthier, O. Hernandez, M. Ceretti, M. Plazanet, K. Conder, and C. Lamberti, "Lattice dynamics to trigger low temperature oxygen mobility in solid oxide ion conductors," *Journal of the American Chemical Society*, vol. 130, no. 47, pp. 16 080–16 085, 2008.

[28] Z. Wang, R. Peng, W. Zhang, X. Wu, C. Xia, and Y. Lu, "Oxygen reduction and transport on the la1-xsrxco1-yfeyo3-δ cathode in solid oxide fuel cells: a first-principles study," *Journal of Materials Chemistry A*, vol. 1, no. 41, pp. 12 932–12 940, 2013.

[29] R. O. Jones and O. Gunnarsson, "The density functional formalism, its applications and prospects," *Reviews of Modern Physics*, vol. 61, no. 3, p. 689, 1989.

[30] S. B. Adler, J. Lane, and B. Steele, "Electrode kinetics of porous mixed-conducting oxygen electrodes," *Journal of the Electrochemical Society*, vol. 143, no. 11, pp. 3554–3564, 1996.

[31] V. Yurkiv, R. Costa, Z. Ilhan, A. Ansar, and W. G. Bessler, "Impedance of the surface double layer of lscf/cgo composite cathodes: an elementary kinetic model," *Journal of The Electrochemical Society*, vol. 161, no. 4, pp. F480–F492, 2014.

[32] J. Fleig, "On the current-voltage characteristics of charge transfer reactions at mixed conducting electrodes on solid electrolytes," *Physical Chemistry Chemical Physics*, vol. 7, no. 9, pp. 2027–2037, 2005.

[33] A. C. van Duin, B. V. Merinov, S. S. Han, C. O. Dorso, and W. A. Goddard Iii, "Reaxff reactive force field for the y-doped bazro3 proton conductor with applications to diffusion rates for multigranular systems," *The Journal of Physical Chemistry A*, vol. 112, no. 45, pp. 11 414–11 422, 2008.

[34] B. Merinov and W. Goddard III, "Proton diffusion pathways and rates in y-doped bazro3 solid oxide electrolyte from quantum mechanics," *The Journal of chemical physics*, vol. 130, no. 19, p. 194707, 2009.

[35] P. G. Sundell, M. E. Björketun, and G. Wahnström, "Thermodynamics of doping and vacancy formation in bazro3 perovskite oxide from density functional calculations," *Physical Review B*, vol. 73, no. 10, p. 104112, 2006.

[36] P. Ferrin, S. Kandoi, A. U. Nilekar, and M. Mavrikakis, "Hydrogen adsorption, absorption and diffusion on and in transition metal surfaces: A dft study," *Surface science*, vol. 606, no. 7, pp. 679–689, 2012.

[37] G. Kresse and J. Hafner, "Ab initio molecular dynamics for open-shell transition metals," *Physical Review B*, vol. 48, no. 17, p. 13115, 1993.

[38] G. Kresse and J. Furthmüller, "Efficient iterative schemes for ab initio total-energy calculations using a plane-wave basis set," *Physical review B*, vol. 54, no. 16, p. 11169, 1996.

[39] G. Kresse and J. Furthmüller, "Efficiency of ab-initio total energy calculations for metals and semiconductors using a plane-wave basis set," *Computational materials science*, vol. 6, no. 1, pp. 15–50, 1996.

[40] V. I. Anisimov, J. Zaanen, and O. K. Andersen, "Band theory and mott insulators: Hubbard u instead of stoner i," *Physical Review B*, vol. 44, no. 3, p. 943, 1991.

[41] S. Dudarev, G. Botton, S. Savrasov, C. Humphreys, and A. Sutton, "Electron-energy-loss spectra and the structural stability of nickel oxide: An lsda+u study," *Physical Review B*, vol. 57, no. 3, p. 1505, 1998.

[42] A. Liechtenstein, V. Anisimov, and J. Zaanen, "Density-functional theory and strong interactions: Orbital ordering in mott-hubbard insulators," *Physical Review B*, vol. 52, no. 8, p. R5467, 1995.

[43] J. P. Perdew, K. Burke, and M. Ernzerhof, "Generalized gradient approximation made simple," *Physical review letters*, vol. 77, no. 18, p. 3865, 1996.

[44] P. E. Blöchl, "Projector augmented-wave method," *Physical review B*, vol. 50, no. 24, p. 17953, 1994.

[45] G. Kresse and D. Joubert, "From ultrasoft pseudopotentials to the projector augmented-wave method," *Physical Review B*, vol. 59, no. 3, p. 1758, 1999.

[46] A. M. Ritzmann, A. B. Munoz-García, M. Pavone, J. A. Keith, and E. A. Carter, "Ab initio dft+ u analysis of oxygen vacancy formation and migration in la1-xsrxfeo3-δ (x= 0, 0.25, 0.50)," *Chemistry of Materials*, vol. 25, no. 15, pp. 3011–3019, 2013.

[47] A. M. Ritzmann, M. Pavone, A. B. Muñoz-García, J. A. Keith, and E. A. Carter, "Ab initio dft+u analysis of oxygen transport in lacoo3: the effect of co3+ magnetic states," *Journal of Materials Chemistry A*, vol. 2, no. 21, pp. 8060–8074, 2014.

[48] A. M. Ritzmann, J. M. Dieterich, and E. A. Carter, "Density functional theory+u analysis of the electronic structure and defect chemistry of lscf (la0.5sr0.5co0.25fe0.75o3-δ)," *Physical Chemistry Chemical Physics*, vol. 18, no. 17, pp. 12 260–12 269, 2016.

[49] P. P. Dholabhai, J. B. Adams, P. Crozier, and R. Sharma, "A density functional study of defect migration in gadolinium doped ceria," *Physical Chemistry Chemical Physics*, vol. 12, no. 28, pp. 7904–7910, 2010.

[50] G. Henkelman, B. P. Uberuaga, and H. Jónsson, "A climbing image nudged elastic band method for finding saddle points and minimum energy paths," *The Journal of chemical physics*, vol. 113, no. 22, pp. 9901–9904, 2000.

[51] G. Henkelman, A. Arnaldsson, and H. Jónsson, "A fast and robust algorithm for bader decomposition of charge density," *Computational Materials Science*, vol. 36, no. 3, pp. 354–360, 2006.

[52] H. J. Monkhorst and J. D. Pack, "Special points for brillouin-zone integrations," *Physical review B*, vol. 13, no. 12, p. 5188, 1976.

[53] J. Lane and J. Kilner, "Measuring oxygen diffusion and oxygen surface exchange by conductivity relaxation," *Solid State Ionics*, vol. 136, pp. 997–1001, 2000.

[54] J. Lane, S. Benson, D. Waller, and J. Kilner, "Oxygen transport in la0.6sr0.4co0.2fe0.8o3-δ," *Solid State Ionics*, vol. 121, no. 1, pp. 201–208, 1999.

[55] A. P and P. J. D, "Physical chemistry, 9st edition," 2010.

[56] C. T. Campbell and J. R. Sellers, "The entropies of adsorbed molecules," *Journal of the American Chemical Society*, vol. 134, no. 43, pp. 18 109–18 115, 2012.

[57] C. T. Campbell and J. R. Sellers, "Enthalpies and entropies of adsorption on well-defined oxide surfaces: Experimental measurements," *Chemical reviews*, vol. 113, no. 6, pp. 4106–4135, 2013.

[58] S. Suthirakun, S. C. Ammal, A. B. Munoz-García, G. Xiao, F. Chen, H.-C. zur Loye, E. A. Carter, and A. Heyden, "Theoretical investigation of h2 oxidation on the sr2fe1.5mo0.5o6 (001) perovskite surface under anodic solid oxide fuel cell conditions," *Journal of the American Chemical Society*, vol. 136, no. 23, pp. 8374–8386, 2014.

[59] E. Bucher, W. Sitte, G. Caraman, V. Cherepanov, T. Aksenova, and M. Ananyev, "Defect equilibria and partial molar properties of (la, sr)(co, fe)o3-δ," *Solid State Ionics*, vol. 177, no. 35, pp. 3109–3115, 2006.

[60] D. Gryaznov, S. Baumann, E. Kotomin, and R. Merkle, "Comparison of permeation measurements and hybrid density-functional calculations on oxygen vacancy transport in complex perovskite oxides," *The Journal of Physical Chemistry C*, vol. 118, no. 51, pp. 29 542–29 553, 2014.

[61] M. Kuhn, Y. Fukuda, S. Hashimoto, K. Sato, K. Yashiro, and J. Mizusaki, "Oxygen nonstoichiometry and thermo-chemical stability of perovskite-type la0.6sr0.4co1-yfeyo3-δ (y= 0, 0.2, 0.4, 0.5, 0.6, 0.8, 1) materials," *Journal of The Electrochemical Society*, vol. 160, no. 1, pp. F34–F42, 2013.

[62] S. Bishop, K. Duncan, and E. Wachsman, "Surface and bulk defect equilibria in strontium-doped lanthanum cobalt iron oxide," *Journal of The Electrochemical Society*, vol. 156, no. 10, pp. B1242–B1248, 2009.

[63] A. Jun, S. Yoo, O.-h. Gwon, J. Shin, and G. Kim, "Thermodynamic and electrical properties of ba0.5sr0.5co0.8fe0.2o3-δ and la0.6sr0.4co0.2fe0.8o3-δ for intermediate-temperature solid oxide fuel cells," *Electrochimica Acta*, vol. 89, pp. 372–376, 2013.

[64] J. Druce, H. Tellez, M. Burriel, M. Sharp, L. Fawcett, S. Cook, D. McPhail, T. Ishihara, H. Brongersma, and J. Kilner, "Surface termination and subsurface restructuring of perovskite-based solid oxide electrode materials," *Energy & Environmental Science*, vol. 7, no. 11, pp. 3593–3599, 2014.

[65] K. Chen, N. Li, N. Ai, Y. Cheng, W. D. Rickard, and S. P. Jiang, "Polarization-induced interface and sr segregation of in situ assembled la0.6sr0.4co0.2fe0.8o3-δ electrodes on y2o3-zro2 electrolyte of solid oxide fuel cells," *ACS applied materials & interfaces*, vol. 8, no. 46, pp. 31 729–31 737, 2016.

[66] R. Kiebach, W.-W. Zhang, W. Zhang, M. Chen, K. Norrman, H.-J. Wang, J. R. Bowen, R. Barfod, and P. V. Hendriksen, "Stability of la0.6sr0.4co0.2fe0.8o3/ce0.9gd0.1o2 cathodes during sintering and solid oxide fuel cell operation," *Journal of Power Sources*, vol. 283, pp. 151–161, 2015.

[67] F. Wang, M. Nishi, M. E. Brito, H. Kishimoto, K. Yamaji, H. Yokokawa, and T. Horita, "Sr and zr diffusion in lscf/10gdc/8ysz triplets for solid oxide fuel cells (sofcs)," *Journal of Power Sources*, vol. 258, pp. 281–289, 2014.

[68] "http://www.openfoam.com/," 2011.

[69] N. Tsvetkov, Q. Lu, L. Sun, E. J. Crumlin, and B. Yildiz, "Improved chemical and electrochemical stability of perovskite oxides with less reducible cations at the surface," *Nature materials*, vol. 15, no. 9, 2016.

[70] J. Mizusaki, M. Hasegawa, K. Yashiro, H. Matsumoto, and T. Kawada, "Nonstoichiometry of the perovskite-type solid solution la0.9ca0.1cr1-yalyo3-δ," *Solid state ionics*, vol. 177, no. 19, pp. 1925–1928, 2006.

[71] Y.-L. Lee, J. Kleis, J. Rossmeisl, Y. Shao-Horn, and D. Morgan, "Prediction of solid oxide fuel cell cathode activity with first-principles descriptors," *Energy & Environmental Science*, vol. 4, no. 10, pp. 3966–3970, 2011.

[72] A. Donazzi, M. Maestri, and G. Groppi, "A multistep model for the kinetic analysis of the impedance spectra of a novel mixed ionic and electronic conducting cathode," *Electrochimica Acta*, vol. 222, pp. 1029–1044, 2016.

[73] E. M. Hopper, E. Perret, B. J. Ingram, H. You, K.-C. Chang, P. M. Baldo, P. H. Fuoss, and J. A. Eastman, "Oxygen exchange in la0.6sr0.4co0.2fe0.8o3-δ thin-film heterostructures under applied electric potential," *The Journal of Physical Chemistry C*, vol. 119, no. 34, pp. 19 915–19 921, 2015.

[74] G. M. Rupp, A. K. Opitz, A. Nenning, A. Limbeck, and J. Fleig, "Real-time impedance monitoring of oxygen reduction during surface modification of thin film cathodes," *Nature Materials*, vol. 16, no. 6, pp. 640–645, 2017.

[75] G. M. Rupp, A. Schmid, A. Nenning, and J. Fleig, "The superior properties of la0.6ba0.4coo3-δ thin film electrodes for oxygen exchange in comparison to la0.6sr0.4coo3-δ," *Journal of The Electrochemical Society*, vol. 163, no. 6, pp. F564–F573, 2016.

[76] F. S. Baumann, J. Fleig, H.-U. Habermeier, and J. Maier, "Impedance spectroscopic study on well-defined (la, sr)(co, fe)o3-δ model electrodes," *Solid State Ionics*, vol. 177, no. 11, pp. 1071–1081, 2006.

[77] Y. Yamazaki, F. Blanc, Y. Okuyama, L. Buannic, J. C. Lucio-Vega, C. P. Grey, and S. M. Haile, "Proton trapping in yttrium-doped barium zirconate," *Nature materials*, vol. 12, no. 7, pp. 647–651, 2013.

[78] K. Nomura and H. Kageyama, "Transport properties of ba(zr0.8y0.2)o3-δ perovskite," *Solid State Ionics*, vol. 178, no. 7, pp. 661–665, 2007.

[79] T. Somekawa, Y. Matsuzaki, Y. Tachikawa, H. Matsumoto, S. Taniguchi, and K. Sasaki, "Physicochemical properties of proton-conductive ba (zr0.1ce0.7y0.1yb0.1)o3-δ solid electrolyte in terms of electrochemical performance of solid oxide fuel cells," *International journal of hydrogen energy*, vol. 41, no. 39, pp. 17 539–17 547, 2016.

[80] T. Tauer, R. O'Hayre, and J. W. Medlin, "An ab initio investigation of proton stability at bazro3 interfaces," *Chemistry of Materials*, vol. 26, no. 17, pp. 4915–4924, 2014.